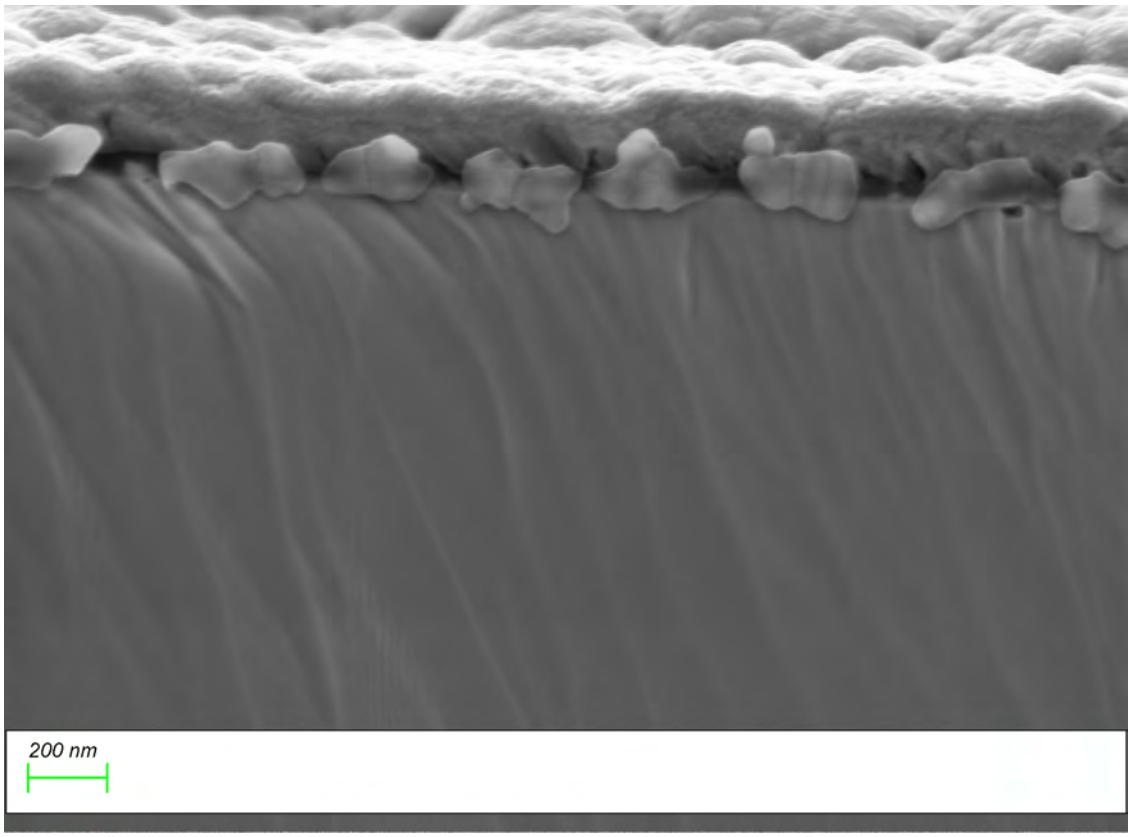

Evaluation of Candidate Materials for Chemical Looping Combustion Fuel Reactor Superheaters

Corrosion Behavior of Fe- and Ni-Based Alloys in Simulated Fuel Reactor Environments at 400°C

Master's thesis in Materials Chemistry

Igor Mitrović, Nils Fredriksson

Division of Materials Chemistry, Department of Chemistry and Chemical Engineering

CHALMERS UNIVERSITY OF TECHNOLOGY

Gothenburg, Sweden 2026

www.chalmers.se

Master's thesis 2026

Evaluation of Candidate Materials For Chemical Looping Combustion Fuel Reactor Superheaters

Corrosion Behavior of Fe- and Ni-Based Alloys in Simulated Fuel Reactor Environments at 400°C

Igor Mitrović, Nils Fredriksson

CHALMERS
UNIVERSITY OF TECHNOLOGY

Department of Chemistry and Chemical Engineering
Division of Materials Chemistry
Chalmers University of Technology
Gothenburg, Sweden 2026

Evaluation of Candidate Materials For Chemical Looping Combustion Fuel Reactor Superheaters
Corrosion Behavior of Fe- and Ni-Based Alloys in Simulated Fuel Reactor Environments at 400°C
Igor Mitrović, Nils Fredriksson

Supervisor: Hooman Karimi Abadeh, Division of Materials Chemistry, Department of Chemistry and Chemical Engineering
Examiner: Jesper Liske, Division of Materials Chemistry, Department of Chemistry and Chemical Engineering

Master's Thesis 2026
Department of Chemistry and Chemical Engineering
Division of Materials Chemistry
Chalmers University of Technology
SE-412 96 Gothenburg
Telephone +46 31 772 1000

Cover: Scanning electron microscopy (SEM) image of the oxide scale formed on Sanicro 28 after exposure to a high-temperature corrosion environment representative of waste-fired chemical looping combustion systems.

Typeset in LaTeX
Printed by Chalmers Reproservice
Gothenburg, Sweden 2026

Corrosion Behaviour of Fe- and Ni-Based Alloys in Simulated Fuel Reactor Environments at 400°C
Influence of KCl Deposits on Protective Oxide Formation and Mass Gain
Igor Mitrović, Nils Fredriksson
Department of Chemistry and Chemical Engineering
Chalmers University of Technology

Abstract

Chemical looping combustion (CLC) is a promising technology, enabling effective carbon capture and storage while reducing the energy penalty associated with carbon capture and storage in conventional waste-to-energy systems. The fuel reactor (FR) side of a waste-fired CLC system exhibits a harsh oxidizing environment; consequently, the material selection is essential for achieving reliable long term operation. This thesis has evaluated the corrosion resistance of six candidate superheater materials for use in the FR of a CLC system. The investigated alloys were Sanicro 28, Sanicro 35, Sanicro 60, TP347, EF101, and a low-alloyed reference steel T22, also used for method development. The samples were exposed for 168 hours at 400°C in an atmosphere containing 5% O_2, 20% H_2O and CO_2 bal. Potassium chloride was deposited on the sample surfaces to simulate the alkali chloride-containing environment associated with the combustion of waste-derived fuels. Using gravimetric analysis combined with scanning electron microscopy (SEM) and energy dispersive spectroscopy (EDS) the corrosion behavior was analyzed.
Results show that Sanicro 28, 35, and 60 exhibit the lowest mass gains and formed thin protective scales with no visible sign of internal oxidation. TP347 also demonstrated good corrosion resistance, although evidence of internal oxidation was observed. EF101 experienced breakaway corrosion along with T22 although spallation was not observed to the same degree. Cross-sectional analysis showed that the Ni-containing alloys were able to form a thin and protective oxide scale which is likely composed of a chromium-rich oxide, while EF101 failed to establish and maintain a continuous protective Al-rich oxide scale, resulting in the formation of Fe- and Cr-rich corrosion products. Chlorine enrichment within the oxide scales also suggest that chlorine induced degradation through the electrochemical mechanism contributed to higher degradation of the metals.
The results indicate that all Sanicro samples along with TP347 are viable candidate materials for use in superheaters in CLC systems. Considering both corrosion performance and alloy composition, TP347 emerges as the most economical alternative due to its lower Ni content, providing a significant improvement in corrosion resistance compared to T22.

Acknowledgements

We would like to take this opportunity to acknowledge the people who have made this thesis possible and have contributed to our growth both academically during our thesis here at Chalmers University of Technology.

First we would like to thank our examiner Dr. Jesper Liske and our Supervisor Hooman Karimi Abadeh, for their guidance, support, and encouragement throughout our thesis project. Your expertise, insights, and constructive feedback have been instrumental in the quality of our work. Furthermore, thank you Dr. Jesper Liske, Hooman Karimi Abadeh, Dr. Maria Paz Olausson, Dr. Hampus Lindmark, and Dr. Torbjörn Jonsson for all the help and advice, and thank you for making us feel welcome and more like colleagues in the work group than students.

We would like to extend our sincere thanks to the division for the collaborative and welcoming atmosphere that enriched our experience. The camaraderie, fun, and laughter we shared have made this journey not only productive but also enjoyable.

We would also like to extend our sincere thanks to the CMAL staff for providing knowledge and helping operate the wide variety of analytical instruments, and the administrative staff, whose assistance has given us the opportunity to access all the necessary facilities.

Thank you all once again. This would not have been possible without your collective support and encouragement. We are grateful for the opportunity to complete our master's studies with such an interesting thesis.

Igor Mitrović, Nils Fredriksson, Gothenburg, June 2026

List of Acronyms

Below is the list of acronyms that have been used throughout this thesis listed in alphabetical order:

AR	Air Reactor
BIB	Broad Ion Beam
BSE	Backscattered Electrons
CLC	Chemical Looping Combustion
DFBR	Dual Fluidized Bed Reactor
EDS	Energy-Dispersive X-ray Spectroscopy
FBB	Fluidized Bed Boiler
FR	Fuel Reactor
HTC	High Temperature Corrosion
MO	Metal Oxide
NIMBY	Not In My Back Yard
OC	Oxygen Carrier
PPBR	Parallel Packed Bed Reactor
SE	Secondary Electrons
SEM	Scanning Electron Microscope
WtE	Waste to Energy

Contents

List of Figures

List of Tables

1
Introduction

1.1 Background

Both biomass- and waste-fired boilers with the possibility of carbon capture and storage have emerged as promising alternatives during the transition from fossil to renewable fuel sources. With the increasing energy demand caused by rapid industrialization, electrification of vehicles and other transport, the need for clean energy is increasingly important [1]. Chemical looping combustion (CLC) displays potential as a solution to long-standing issues of carbon capture in boiler systems: the energy-intensive separation of large amounts of N_2 present in air, from CO_2, a crucial step to isolate CO_2 in the exhaust gas for carbon capture. CLC operates through the use of two reactors: an air reactor (AR), where air is used to regenerate oxygen carriers (OC), and a fuel reactor (FR), where OCs are used as the fluidization bed for combustion in a steam atmosphere [2]. By separating the combustion process from the air supply, the resulting flue gas becomes largely nitrogen-free, reducing the separation required prior to permanent storage and enabling net-negative CO_2 emissions when using biomass and municipal waste fuels [2]. Due to the novelty of CLC and its unique flue gas composition, along with the flue gas complexity in waste-fired boiler systems, not much is known about the corrosivity of different superheater materials in CLC systems. As such, investigation of corrosion of different steels as superheater material in a simulated waste-fired FR environment becomes relevant.

1.2 Aim

The aim is to develop a robust and repeatable exposure methodology for laboratory testing in simulated fuel reactor environment, and to investigate the corrosivity of six different alloys as superheater material in the fuel reactor side of chemical looping combustion waste-fired boilers. To assess the corrosivity, evaluation and comparison of the materials' oxidation behavior and oxide scale morphology and microstructure will be in focus.

1.3 Limitations

Exposures will be performed in laboratory scale furnace setups rather than in operating boiler systems. This makes the results less representative of real service conditions than tests performed in full-scale boiler environments. The true extent

of corrosion cannot be fully investigated, as superheater material in real world applications is exposed to different environments on the tube exterior and interior (the so-called "fire side" and "steam side", respectively). The current experimental setup does not allow for dual-atmosphere exposure, it is assumed that both flue gas and KCl environments affect both sides of the material. This simplification may not accurately represent the coupled effects of internal and external corrosion processes observed in service conditions. Samples will only be weighed before and after exposures, making determination of oxidation kinetics and rate laws impossible. In addition, chromium evaporation was not quantified, which introduces uncertainty into the mass change measurements and may result in an underestimation of the true extent of corrosion.

2

Theory

2.1 Boiler Systems

Corrosion is a major challenge in boiler system applications, causing personal injury, reducing equipment lifespan, and costing 3-4% of global GDP annually [3]. Because corrosion is environment-dependent and the environment itself depends on factors such as fuel, input gas, and boiler design; it is important to understand the boiler environment in order to understand the corrosion processes occurring within it. Boilers were first developed at the end of the 1600s [4]. These early boilers were essentially composed of a furnace in which fuel was combusted in order to boil water contained in an enclosed pot above the fire [4]. The volume expansion of water to steam was used to drive pistons in early industrial pumps and other machinery [4]. Since then, the concept of boilers has been developed into several modern iterations in use today. Unlike in a non-fluidized boiler where a fixed bed, in which the fuel is housed, sits at the bottom of the reactor, in a fluidized bed boiler (FBB) the bed consists of particulate matter, often sand and ash [5]. The bed material is fluidized by passing a gas, often air, through it at velocity sufficient to lift the bed particles, causing the bed to behave like a turbulent fluid, instead of solid particles [5]. The fuel is mixed with the bed material in a ratio of 1-5% fuel to total solid bed mass and the fuel is combusted by contact with hot particles in the bed [5]. The thermal capacity of the fluidized bed material gives fast drying and consistent combustion temperature, and the bed has good mixing, giving efficient heat transfer between solid and gas [5]. This allows for simultaneous combustion of several different fuels and results in low sensitivity to fuel quality, allowing for efficient combustion of low-grade fuels with high moisture content, such as municipal waste and bio-fuels [5]. The combustion generates hot flue gas which transfers heat to water flowing through furnace wall tubes, turning the water into steam that then flows into the superheater. The superheater is a heat-exchange system consisting of a series of pipes with steam flowing through them. Flue gas from combustion is directed through the superheater, once again transferring heat to the steam, superheating it [5]. Superheaters are designed for maximum surface area to increase heat transfer from the flue gas to the steam. However, the high surface area means that the superheater is more susceptible to corrosion and deposition buildup, making it a relevant area for study to reduce corrosion.

2.1.1 Waste Fired Boilers

The concept of municipal solid waste incineration is not new; the first use of an incinerator was in the United Kingdom in 1874 with a primary focus on waste management rather than energy recovery [6–9]. It was not until shortly before the twentieth century in Europe and midway through the twentieth century in the US that heat recovery from incinerators began as a result of rising oil prices putting waste to energy (WtE) at the forefront of primary waste treatment design [6]. The use of WtE plants offers a solution not only for renewable energy production but also for the management and reduction of the size of landfills. In both Sweden and Denmark, it has been proven that well established energy generation can be achieved with WtE plants where WtE plants account for approximately 2 TWh of electricity generation and 30% of domestic heat consumption in Sweden with around two million tons of waste imported annually, which avoids land-filling and reduces emissions [7, 10]. Despite this, skepticism around the technology still remains, which is why it has not yet seen as much adoption around the world as in Sweden and Denmark; this is caused by local experiences with emissions from older incineration plants, which have sparked the not-in-my-backyard (NIMBY) movement [9].

In WtE systems, different technologies work together to convert solid waste into electricity and heat. A WtE plant is made up of seven main parts, beginning with waste reception and handling, also called the refuse pit [11, 12]. As the waste moves from the refuse pit, it is transferred to the combustion chamber[8, 11]. As energy is released from the combustion chamber in the form of flue gases, it enters the boiler where energy is recovered [8, 11]. Here, the thermal energy contained in the combustion flue gases is recovered to generate steam for heat and power production. The flue gases utilized in the boiler for power generation are then sent to a treatment system to minimize particulate matter, acid gases and nitrogen oxides in the emissions as they are released into the atmosphere [11].

The primary drawback of WtE plants compared to other boiler systems using fossil fuels is the high temperature corrosion and fouling of the different components caused by alkali metals and other corrosive constituents present in municipal waste [13–15]. As components of WtE plants begin to corrode, the strength and efficiency of components change. Furthermore, if fouling occurs on heat-exchanger surfaces, the ash build-up begins acting as an insulator which lowers the heat transfer efficiency [13, 15–17].
In order to increase the overall efficiency of a WtE plant, chemical looping combustion (CLC) technology offers a reduced cost and energy penalty for carbon capture and storage (CCS) and reduces environmental pollutants compared to conventional incineration of municipal waste [18–21].

2.1.2 Chemical Looping Combustion

The combustion process in CLC takes place in dual-reactor setup, with the use of a FR and an AR [18, 20–24]. For combustion to occur in the FR, oxygen is transported from the AR using metal oxides as oxygen carriers, the interconnection

between the two reactors allows the transfer of the reduced OC from the FR to the AR where it is oxidized from Me_xO_{y-1} to form Me_xO_y. By preventing direct contact between fuel and air a FR environment almost void of nitrogen gas can be achieved, which produces a CO_2-rich flue gas stream as fuel and oxygen supplied from the OC combusts, which allows for easy separation and purification of CO_2 for permanent storage or production of carbon-based value-added materials[18, 20–24]. CLC offers a thermodynamic advantage over post-combustion carbon capture and storage, by separating CO_2 from NO_x compounds through the supply of oxygen with OC, the high energy penalty associated with solvent regeneration is therefore avoided [25–30]. Additionally, the higher temperature environment of AR, caused by the oxidation of OC materials has the potential to produce electricity at a higher efficiency, even comparable to state-of-the-art coal-fired boilers [31]. Furthermore, the use of carriers in chemical looping is not limited to oxygen, but can also be used for CO_2, nitrogen, and even sulfur carriers, allowing for broad application within calcium looping, chemical looping ammonia synthesis, and chemical looping desulfurization [2, 18, 20–24, 32, 33].

When designing an FR the primary goal is to achieve full conversion of the MSW by increasing contact between the OC particles and the fuel, along with adjusting critical reaction parameters such as pressure, temperature, and product gas composition [33–36]. Depending on the involvement of OC in the oxidation-reduction reactions, the configuration of the CLC reactor can be categorized into two types, one with a dual reactor set-up where the oxidation and reduction of circulating OC take place in separate reactors and one where the reaction takes place within the same reactor with a stationary OC and alternating atmosphere [24, 37]. CLC plants that use a dual reactor design with circulating OC usually use a dual fluidized bed reactor (DFBR) or a dual circulating fluidized bed reactor (DCFBR) set-up [2, 22, 24, 33, 37–39]. For plants using a single reactor set-up, a parallel packed bed reactor (PPBR) or rotary reactors are used [2, 24, 38]. The choice of reactor depends on the fuel source and combustion mode, making it applicable in different scenarios [24, 38]. Most CLC reactors reported in the literature, as well as most pilot-scale plants, employ a DFBR configuration, this is due to their high efficiency of fuel conversion along with long cycle operation, ease of industrial scale-up, and the ability to use a wide range of fuels; this allows for gas fuel CLC, syngas-CLC and solid fuel in-situ gasification CLC [2, 24, 38].

The choice of OC material for CLC is critical as it acts as the bridge for oxygen transport to the FR. The physical and chemical properties of the OC material affect the performance, efficiency, and cost of the entire CLC process. The performance of an oxygen carrier is determined by their reactivity with the fuel, oxygen transport capacity, chemical lifetime, mechanical resistance, tendency to carbon deposition on their surface, toxicity and environmental impact, price and availability, resistance to fragmentation and attrition, along with low tendency for agglomeration [2, 32, 34–36, 40]. When talking about OC, they can be categorized into natural OC (ilmenite) and synthetic OC ($Cu_{0.95}Fe_{1.05}AlO_4$), they can also be classified based on properties such as the number of active compounds, structure, and the ability to uncouple oxygen in the FR [2, 34]. Promising strides in organic OC have been made recently,

with OC based on geopolymer composites being proposed, with the main advantage of low cost, green synthesis and non-toxic, along with good mechanical strength with applications in fluidized bed reactors [2].
Although CLC offers a promising high efficiency pathway for CO_2 capture, it faces challenges related to OC degradation through attrition, sintering and agglomeration along with challenges involving reaction scale-up and high-temperature corrosion of the superheater material used for district heating and power generation [2, 21, 31, 33, 36, 41, 42]. Superheater tubes are usually made from low-alloy carbon steels due to their low cost and good mechanical properties [31]. Although cost-effective, carbon-steel tube material in FR offers low corrosion resistance in harsh environments that contain alkali metal compounds and chlorinated compounds such as KCl and HCl caused by variation in feedstock quality [21, 22, 31, 33, 36, 42]. Minimizing the extent of high temperature corrosion of superheaters improves electrical efficiency, extends the life of the components, and reduces maintenance costs [31, 43]. To mitigate the corrosion of superheater material, alloys with higher corrosion resistance than that of carbon steel could be used, another method is to apply corrosion resistant coatings or weld overlays [31, 43].

2.2 Corrosion & Scale Growth

Corrosion can refer to any process that structurally degrades a material, but corrosion of metals specifically refers to the conversion of pure metals or alloys into ions and the subsequent formation of oxides, driven by a reduction in Gibbs free energy [44]. Corrosion and its prevention are important topics as corrosion and its products lead to reduction in heat transfer efficiency, structural degradation and failure. In boiler systems, temperatures often exceed 100°C and corrosion occurring under such conditions, known as high-temperature corrosion (HTC), is therefore of particular interest. Corrosion of metals is driven by a reduction in energy, but this is not enough to understand how corrosion happens. At its core, corrosion is a redox reaction. In HTC, the first part of the redox reaction is the oxidation of the metal into metal ions. There are several potential oxidants, but the most common one is $O_2(g)$ which is reduced to O^{2-} as it chemisorbs to a metal surface, constituting the second part of the reaction [45].

$$\begin{aligned} \mathrm{M} &\longrightarrow \mathrm{M}^{2+} + 2\,\mathrm{e}^- && \text{(oxidation)} \\ \frac{1}{2}\,\mathrm{O_2} + 2\,\mathrm{e}^- &\longrightarrow \mathrm{O}^{2-} && \text{(reduction)} \\ \mathrm{M} + \frac{1}{2}\,\mathrm{O_2} &\longrightarrow \mathrm{MO} && \text{(overall reaction)} \end{aligned}$$

As seen above, the overall reaction produces a metal oxide (MO). It is important to note that the oxidation and reduction occur simultaneously in the form of the overall reaction. Assuming the oxidation is relatively homogeneous over the surface, a layer of oxide, also called a scale, will form. After a scale has formed, further oxidation of the metal is governed by the diffusion of oxygen and metal ions, as well as electrons through the scale [45]. For most metal oxides, the slower of these processes is ion

diffusion, causing it to be the rate-controlling step and the main way in which an oxide scale may protect the underlying metal [45]. However, for the scale to be considered protective, it must be thin, slow growing and sufficiently decrease the rate of diffusion such that diffusion through the scale, rather than surface reaction rate, becomes the rate controlling step. If the scale does not sufficiently reduce the diffusion rate, it will not slow down further corrosion of the metal and cannot be considered protective. There are several reasons why a scale may not sufficiently reduce diffusion rates, one of which is the presence of defects within the oxide. Like pure metals, metal oxides contain both Schottky and Frenkel defects, and a defect-free material is practically unattainable [45]. A Schottky defect is a combination of vacancies of opposite but equal charges, while a Frenkel defect is the combination of a vacancy and an interstitial ion of the same species [45]. In HTC, vacancies are particularly important because they create points within the oxide lattice that allow for cation migration, thereby facilitating diffusion [45]. Interstitial ion point defects can also promote diffusion, but through a different mechanism, whereby the interstitial ion moves into an occupied lattice position, forcing that position's ion to move to an interstitial position [45]. Defects relate to the rate of diffusion through a material because the rate of diffusion, or diffusion flux (J), is equal to -1 times the concentration gradient ($\frac{dC}{dx}$) multiplied by the diffusion coefficient (D) according to Fick's first law of diffusion (Eq. 2.1) [45]. The diffusion coefficient is dependent on the diffusing species, material, and temperature, and therefore varies significantly between different systems.

$$J = -D\frac{dC}{dx} \tag{2.1}$$

Defects give rise to semiconductor properties of oxides. There are two different types of semiconductor oxides: n-type and p-type. An n-type oxide is one where electrons are charge carriers because of an excess of positive charges due to interstitial cations, or a deficiency in negative charges due to anion vacancies [45]. Conversely, in a p-type oxide, holes are charge carriers because of an excess of negative charges due to interstitial anions, or a deficiency in positive charges due to cation vacancies [45]. This concept does not only apply to semiconductor properties but also to scale growth, where they give rise to differences in rates of diffusion for metals (cations) and oxygen (anions) through the scale. We see outward growth of the scale for metal excess in n-type oxide and cation vacancies in p-type oxide, and inward growth for anion vacancies in n-type oxide and oxygen excess in p-type oxide.

2.2.1 HTC on a Laboratory Scale

Several factors influence scale formation, growth, morphology, and microstructure. These factors include temperature, O_2 partial pressure, H_2O content and the presence of corrosion promoting species, such as alkali chlorides [46]. Alkali chlorides and other species are present in high concentration in waste and bio-fuels, creating a harsh flue gas environment, making the effect of these species on corrosion of interest when investigating such environments [46]. While these factors are true for corrosion on an industrial & laboratory scale, the experimental setup used in

the laboratory may bring additional factors e.g., furnace tube material and pressure which can influence scale morphology and microstructure [47]. Different tube materials and pressures have been shown to influence scale morphology and composition, with higher pressure also increasing chromium evaporation rates [47]. Effects on chromium and chromium evaporation are important to consider since chromium is the main constituent element of protective oxide scales for alloys considered. Removal of chromium thus results in scale breakdown and loss of protection.

2.2.2 Effects of Alkali Chlorides on HTC

As mentioned in section 2.2.1, alkali chlorides are highly corrosive and present in flue gases from biomass and waste-derived fuels. This makes alkali chlorides an important topic to understand corrosion in waste-fired boiler systems. It has been shown that oxidation of high and low-alloy steels in 5% O_2 and 20 - 40% H_2O forms a slow-growing, uniform scale with hematite whiskers on the surface after exposure at 400°C for 24 h [46, 48]. This scale is 0.5 - 1.4 μm thick and is composed of a bi-layered outward growing scale, itself composed of a thin hematite layer on top of a thicker magnetite layer [46, 48]. An inward growing, chromium-containing spinel was also found in both cases [46, 48]. Similar scale morphology and microstructure was found after 168 h [46]. Furthermore, KCl deposition on samples before exposure has been shown to yield a 5.5 - 7.5 μm thick scale composed of a corundum, a spinel and maghemite (γ-Fe_2O_3) which has the same crystal structure as magnetite but the chemical formula of hematite [48]. After exposure for 24 h, unreacted KCl crystals, some overgrown by the scale, covered nearly 20% of the surface in the form of single crystals and agglomerates [48]. KCl also caused cracks to form on the sample surface and oxidation in these cracks [48]. As described, KCl will contribute to accelerated corrosion, changed oxide microstructure, reduced oxide cohesion and increased relative amount of inward growing oxide. This is attributed to small amounts of potassium and chlorine inside the scale increasing the rate of oxygen diffusion and chlorine accumulation at the metal/oxide interface due to migration of chlorine from the surface during salt particle breakdown [46]. Breakdown leading to chlorine release may also lead to HCl formation, further harshening the flue gas environment [46]. While it is clear that chlorides are highly corrosive in a high-temperature environment, the exact mechanism of alkali chloride corrosivity is still debated and several mechanisms have been proposed [48–50]. It has been argued that Cl_2 is the only corrosive species in alkali chlorides that catalyzes the formation of metal oxides [16, 49, 51]. In this mechanism, it is generated in a reaction between alkali chlorides and O_2 or oxides, allowing the Cl_2 to penetrate the scale and react at the scale/metal interface to generate volatile metal chlorides [16, 49, 51]. As the metal chlorides reach the air/scale interface Cl_2 is regenerated and again able to catalyze the formation of more corrosion products [16]. There is also an electrochemical argument, where Cl^- ions instead penetrate the scale and react at the scale/metal interface and in this mechanism, the alkali ion plays an important role by reacting with the oxide scale and forming K_2CrO_4, causing breakdown of the oxide due to reduced chromium concentration, and loss of primary protection [49]. This specific mechanism for the corrosivity of potassium may not be relevant for

all commercial alloys but since most corrosion resistant alloys contain chromium to form a corrosion resistant chromium rich oxide, the role of potassium is of interest. Another mechanism relevant to alkali chlorides is the lowering of first melting temperature (FTM) of deposits on superheaters, caused by the presence of chloride [50]. Lower FTM leads to higher risk for melting of deposit species and higher partial pressure of corrosive species in the flue gas [50]. This effectively increases corrosivity of the environment due to molten and gas phase species generally having higher reactivity than solid state ones [50].

2.3 Scanning Electron Microscopy

Scanning electron microscopy (SEM) is the primary characterization technique used in this study. Electron microscopy is a non-destructive characterization method that is able to generate high resolution electrograph images, allowing for visualization of surface features at the nanometer scale [52]. To accomplish this, a SEM uses a field emission gun to shoot an electron beam at the sample [52]. These electrons first pass through a series of apertures and electromagnetic lenses, focusing the beam [52]. When the focused beam strikes the sample, the beam electrons interacts with electrons in the sample, scattering electrons away from the sample surface [52]. The scattering can be elastic, generating backscattered electrons (BSE), or inelastic, generating X-rays and secondary electrons (SE). BSEs and SEs are picked up by different detectors in order to generate images with BSEs giving topographic and phase information, and SEs typically giving higher resolution topographic images due to their smaller interaction volume. X-rays are used for chemical characterization of the sample by energy-dispersive X-ray spectroscopy (EDS), giving information on the chemical makeup of the material [52]. The beam electrons are accelerated by high voltage and the interaction volume mentioned before can be made smaller or larger by decreasing or increasing the acceleration voltage of the electron beam [52]. Acceleration voltages of 10 - 20 keV are used in this study. SEM provides many advantages but it still does have some limitations. The primary limitation arises from the need to place the system under vacuum [52]. This is done partly in order to remove interactions between beam electrons and air, but the primary purpose is to remove contaminants that can cause the field emission gun filament to degrade during use [52]. Some sample limitations should also be considered. First, samples need to be relatively small in order to fit into the instrument. Second, the sample must have some level of conductivity, meaning that non-conductive samples, e.g. organic polymer films, must be prepared by gold sputtering before electron microscopy.

2.3.1 Cross-Sectional Sample Preparation

An important sample preparation technique used in this study is broad ion beam (BIB) milling which is commonly used to mill near perfect, artifact free cross-sections of samples for SEM characterization [53–56]. Ion beam milling is done by mounting a sample inside a vacuum chamber and bombarding it with a beam of ions, usually argon, but other ions like iodine and xenon are also used [53, 54]. By applying a mask to the sample beforehand, one can ensure that only a small part of the sample

is milled, creating a cross-sectional view of the sample surface for SEM analysis [53, 55].

3
Materials & Methods

3.1 Materials

The alloys investigated in this study are shown in Table 3.1.

Table 3.1: The chemical composition of investigated alloys [57–62].

Alloy \ Element (wt.%)	Fe	Cr	Ni	Mo	Si	Mn	Cu	Nb	Al	Minor elements
T22	bal.	1.96	×	0.91	0.46	0.35	×	0.7	×	C, P, S, V, Ti
Alleima® TP347	bal.	17.5	10	×	0.6	1.7	×	0.7	×	C, P, S
Sanicro® 28	bal.	27	31	3.5	0.7	2	1	×	×	C, N, P, S
Sanicro® 35	bal.	27	35	6.5	0.5	0.8	0.2	×	×	C, N, P, S
Sanicro® 60	4	21.5	bal.	8.7	0.2	0.2	×	3.5	×	C, P, S
Kanthal® EF101	bal.	11-14	<0.5	×	1-2	<0.7	×	×	3.2-4.2	C

The investigated materials were selected to study a range of candidate alloys for use as superheater materials. T22 was chosen as the benchmark material due to its wide application in boilers, low cost, and well-studied corrosion resistance properties. TP347 was selected as a commercially established austenitic stainless steel commonly used in high-temperature applications. Sanicro 28 and Sanicro 35 were selected as high-alloy stainless steels developed for corrosive boiler environments. Sanicro 28 has been extensively tested and is known for its high corrosion resistance properties, while Sanicro 35 is a newer alloy intended to provide similar resistance properties at lower cost. Sanicro 60 was selected as a highly corrosion-resistant Ni-based alloy and serves as a benchmark for the upper range of corrosion performance achievable with commercially available materials. EF101, a FeCrAl alloy, was included because it is designed to form a protective Al-rich oxide scale. Such alloys have demonstrated high corrosion resistance at elevated temperatures, and EF101 was therefore investigated to evaluate whether similar benefits could be seen under the lower-temperature conditions relevant to the thesis.

3.2 Experimental

Before exposure, the sample edges were polished under water using 1200-grit silicon carbide paper. The samples were then automatically ground using a Struers

Tegramin-30 automatic polishing machine on silicon carbide paper ranging from 500 up to 4000 grit size, followed by polishing with 3 and 1 μm diamond suspensions to obtain a mirror finish. Subsequently, the samples were cleaned by immersion in acetone and ultrasonication for 25 min. KCl was applied to the samples by spraying a supersaturated solution of KCl in a 20:80 deionized water/ethanol mixture onto the samples under continuous drying to achieve a homogeneous coverage and a total KCl deposition of 2 mg/cm^2. Samples were then mounted on a sample holder together with gold coupons used to assess KCl loss during exposure. The samples were arranged such that each sample occupied a center position once in order to assess wall effects, as shown in Figure 3.1.

The gas composition during the exposure was selected to simulate conditions relevant to the fuel reactor of a chemical looping combustion system. CO_2 was used as the balance gas since complete fuel conversion in the fuel reactor ideally produces CO_2 as the primary gaseous combustion product. A steam concentration of 20 vol.% was included to represent the high H_2O partial pressures expected during the combustion of moist fuels and waste-derived fuels. An oxygen concentration of 5 vol.% was included to simulate oxidizing conditions that may arise in the fuel reactor due to oxygen slip from the air reactor through the oxygen carrier particles or through gas mixing between reactor sections. Together, the gas mixture represents a high-steam, CO_2-rich, nitrogen-free environment relevant to fuel reactor superheater applications in CLC systems. The samples were subsequently placed along with a KCl boat in a tube furnace calibrated to 400°C and exposed for 168 h in a 1000 cm^3/min gas flow of 5% O_2 + 20% H_2O + CO_2 bal. After exposure, samples were allowed to cool to room temperature in a desiccator containing SICAPENT© (P_2O_5) and subsequently weighed. The mass gain was then calculated according to the method described in 3.4.

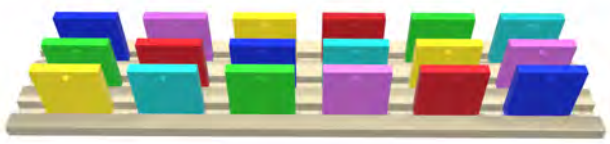

Figure 3.1: Schematic illustration of sample placement on the sample holder

3.2.1 Method Development

Before the exposures described above were carried out, a method development exposure to determine downstream effects on sample corrosion was performed. A total of 18 T22 samples were prepared by polishing and KCl deposition procedure described above. The samples were placed on a sample holder with gold coupons located at the red positions as shown in Figure 3.2 and placed along with a KCl boat in a furnace calibrated to 400°C. The samples were then exposed for 168 h in a 5% O_2 + 20% H_2O + CO_2 bal. gas. After exposure, the samples were allowed to cool to room temperature before being weighed, after which mass gain calculated (see 3.4).

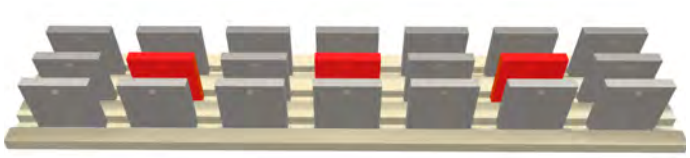

Figure 3.2: Schematic of 21 samples placed on sample holder for method development

3.3 Characterization

The exposed samples were examined for morphological and microstructural characterization using an FEI Quanta 200 ESEM and an LEO Ultra 55 SEM, with an accelerating voltage of 10-20 keV. A Hitachi TM4000 Plus SEM with EDS was used at 15 keV to determine the atomic composition of cross-sections. Similarly, a Phenom ProX Desktop SEM with EDS was used for plan view imaging and atomic composition. For plan view, samples were mounted on a pin stub mount using carbon tape. For cross-sectional analysis, a silica wafer was glued to the scale and left to dry. Subsequently, the samples were cut and polished with $2\mu m$ polishing paper using a Leica EM TXP cross-sectioning device at low speed without lubricant. The cut and polished samples were then mounted onto a stub using silver paint before being subjected to broad ion beam (BIB) milling with triple Ar-guns for 8 h using a Leica EM TIC 3X prior to cross-sectional SEM examination.

3.4 Calculations

Sample mass gain ($\Delta W,\ mg/cm^2$) was calculated by dividing the difference in post-exposure mass ($m_1,\ g$) and pre-exposure mass with KCl ($m_0,\ g$) by the surface area ($A,\ cm^2$), according to equation 3.1.

$$\Delta m = 1000\,\frac{m_1 - m_0}{A} \tag{3.1}$$

Equilibrium calculations for reactions in the furnace-sample system were done using FactSage 8.4.
The theoretical oxide thicknesses seen in Table 4.1 were estimated from the corrected mass gain and assuming uniform oxide growth across the exposed sample surface. The calculated oxide thicknesses were based on approximating the oxide scale as Fe_3O_4 using a density of 5.17 g/cm^3 and the oxygen mass fraction of the oxide.
The oxide thickness was calculated according to

$$t = \frac{\Delta m}{\rho f_O} \times 10^4 \tag{3.2}$$

where t is the oxide thickness (μm), Δm is the corrected mass gain per unit area (g/cm^2), ρ is the density of Fe_3O_4 (5.17 g/cm^3), and f_O is the oxygen mass fraction

in Fe_3O_4. The factor 10^4 converts the calculated thickness from centimetres to micrometres.
The oxygen mass fraction was determined from the stoichiometry of Fe_3O_4 as

$$f_O = \frac{3 \times 16}{3 \times 16 + 4 \times 55.85} = 0.177 \tag{3.3}$$

Substituting the density and oxygen mass fraction into the equation gives

$$t = \frac{\Delta m}{5.17 \times 0.177} \times 10^4 \tag{3.4}$$

The calculated thicknesses should be regarded as theoretical estimates based on simplified assumptions regarding oxide composition and uniform scale growth and were used for comparison with oxide thicknesses measured directly from SEM cross-sections.

4

Results & Discussion

4.1 Method Development

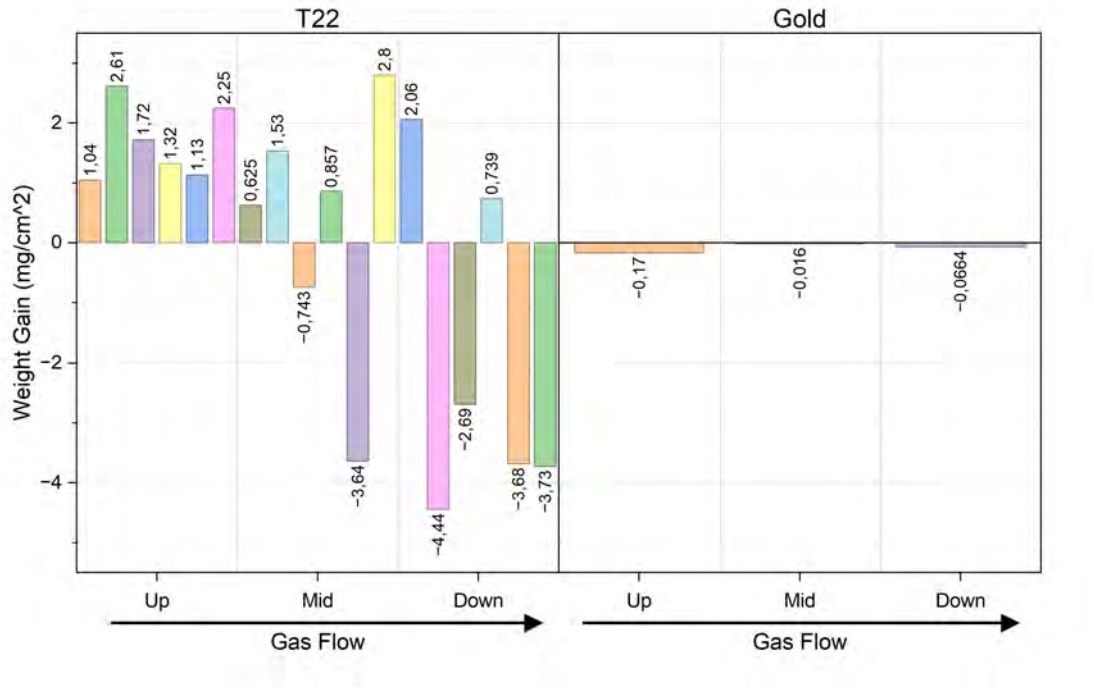

Figure 4.1: Weight change measurement of T22 and Gold samples for method development.

The method development exposure showed inconclusive mass gain results due to severe scale spallation. As can be seen in Figure 4.1, the most severe spallation appears to be localized to the downstream region. However, this is likely due to differences in sample thickness, causing some samples to adhere more strongly to the sample holder and consequently experience more severe spallation during removal. This prevented the use of weight gain measurements to conclusively determine downstream effects. Furthermore, visual inspection revealed similar scale surface morphologies in the upstream, midstream, and downstream regions. Cross-sectional SEM showed a bi-layered scale consisting of an outer hematite on top of an inner magnetite layer (Fig. 4.2), consistent with previous findings. Scale detachment is observed (Fig. 4.2c), beneath which, a new bi-layered hematite/magnetite scale has formed (Fig. 4.2b). The detached scale echibits hematite whiskers characteristic of T22 steel in

similar environments. Unreacted KCl salt crystals are present on the scale surface. Within the detached scale, a void is observed, and a portion of the metal appears to have detached along with the scale and is located at the top of the void (Fig. 4.2d). The original specimen surface cannot be identified in these cross-sectional images.

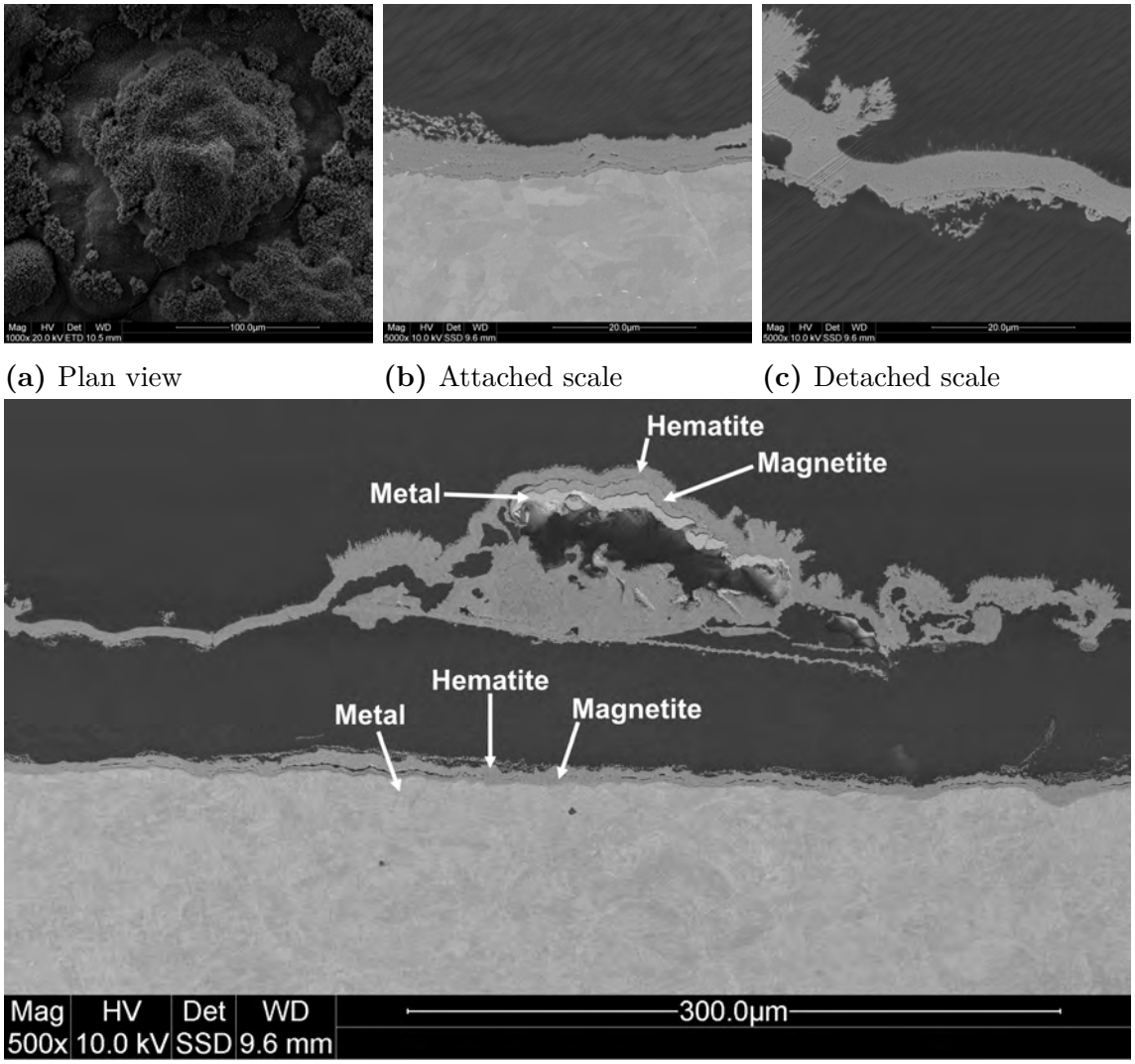

(a) Plan view **(b)** Attached scale **(c)** Detached scale

(d) Attached and detached scale

Figure 4.2: Cross-section of T22 after 168 h exposure

4.2 Gravimetric Analysis

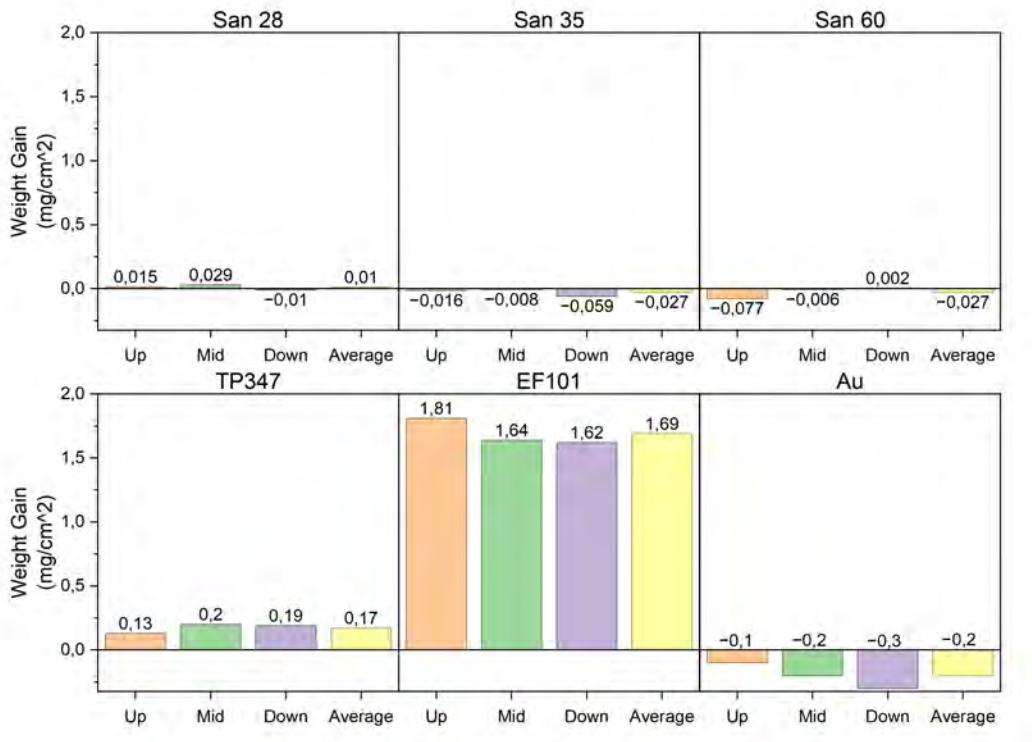

(a) Mean weight gain for samples exposed in Exposure 1, showing upstream, midstream, downstream, and overall average values

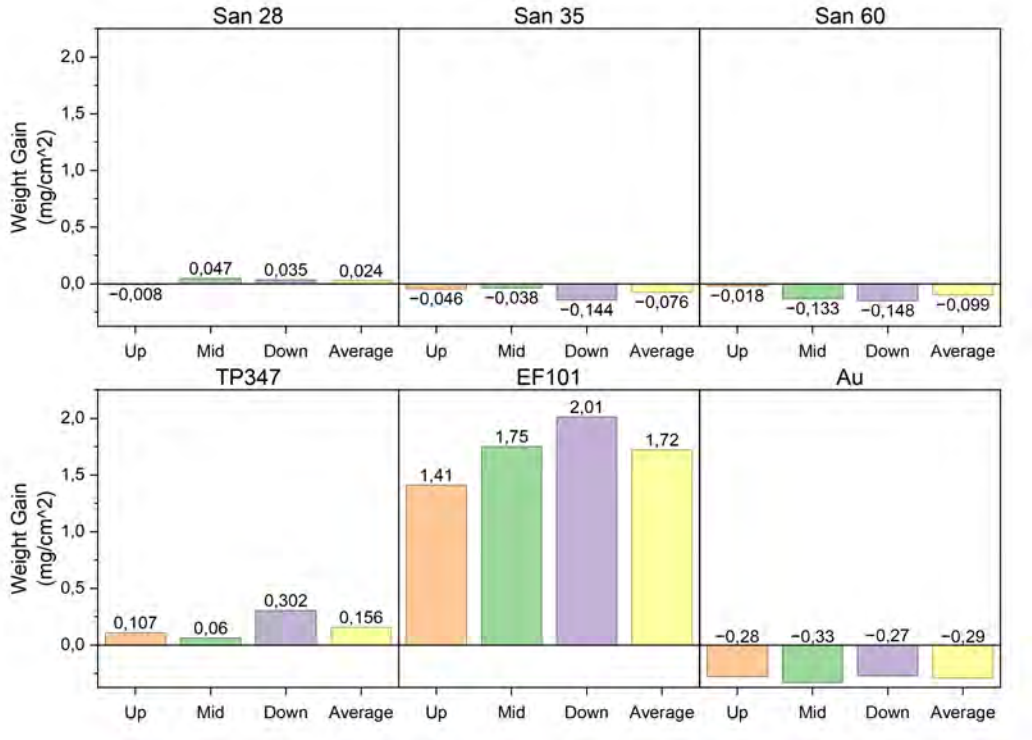

(b) Mean weight gain for samples exposed in Exposure 2, showing upstream, midstream, downstream, and overall average values

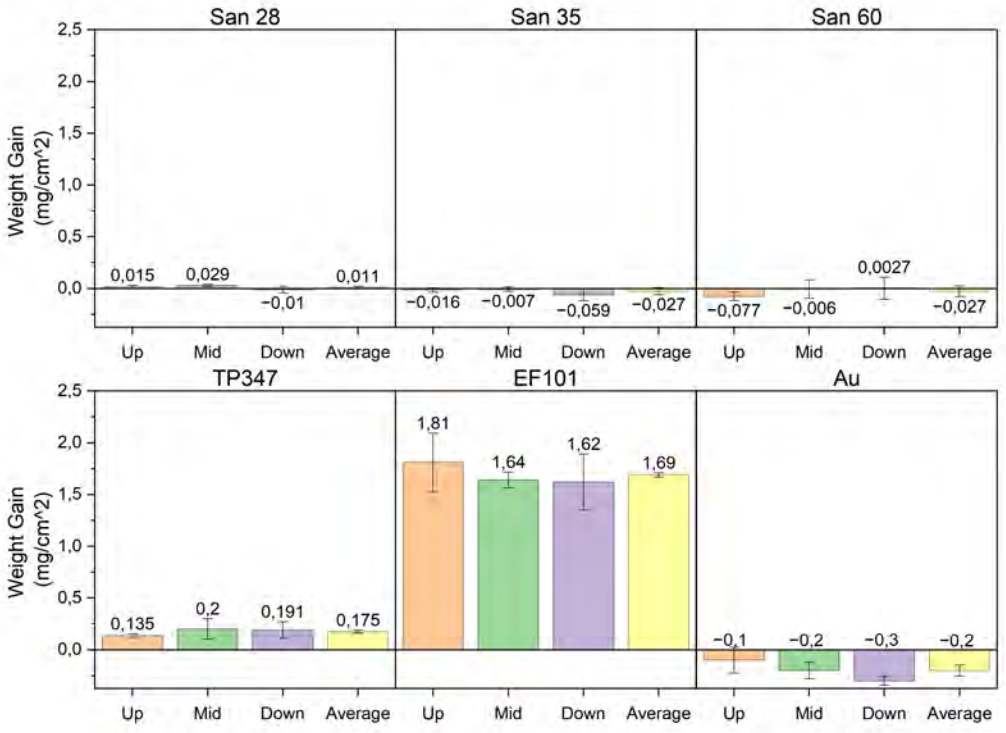

(c) Mean weight gain for samples exposed in Exposure 1 and Exposure 2, with standard deviation, showing upstream, midstream, downstream, and overall average values

Figure 4.3: Weight change measurements for San 28, San 35, San 60, TP347, EF101 and gold samples, exposed to 20% H_2O, a CO_2 flow rate of 950 ml/min, O_2 flow rate of 50 ml/min at 400°C for 168h

Figures 4.3a and 4.3b show the mass change measurements obtained after the samples had been exposed to 5% O_2 + 20% H_2O + CO_2 bal at 400°C for 168 h. No clear systematic differences in mass change were observed between the upstream and downstream positions, nor were any wall effects identified. Sanicro 28, Sanicro 35 and Sanicro 60 all exhibited similarly mass gain, TP347 shows a somewhat higher mass gain, while EF101 shows the highest mass gain compared to the other materials. In 3.1 it can be seen that all materials that show a lower mass gain contain Ni, while EF101, which shows a higher mass gain, is a FeCrAl alloy. This decreased mass gain for NiCr-based alloys may be attributed to the formation of a stable, dense, and adherent passive film likely composed of Cr_2O_3, which suppresses further oxidation by limiting ionic transport. According to the Wagner-type oxidation theory, protective oxidation requires sufficient chromium transport to maintain the formation of an external chromia scale rather than forming a non-protective Fe-rich oxide scale [63]. Although chromium diffusion is slow at 400°C, oxidation kinetics are also reduced compared to higher temperature environments. The low mass gains for the Ni-containing alloys together with their retained metallic appearance suggest that they are able to form a thin protective chromia scale. Since Cr evaporation is expected to be negligible at 400°C, the formation and maintenance are likely primarily controlled by solid-state diffusion rather than chromium evap-

oration. Among NiCr-based alloys, San 28, 35, and 60 show a lower mass change compared to TP347. The difference between these alloys lies mainly in Ni content, with TP347 having the lowest at 10% while San 28, 35, and 60 all have more than 30%. However, based on the gravimetric data, it suggests that increasing the Ni content further above 30% gives a negligible difference in corrosion resistance.

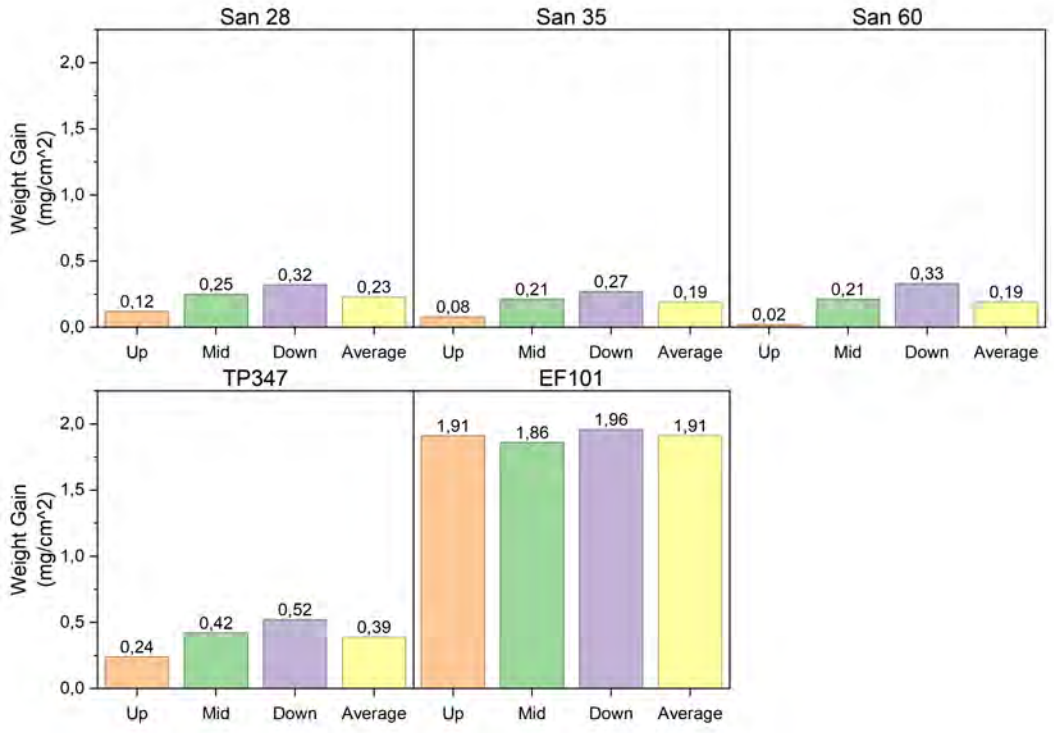

(a) Exposure 1

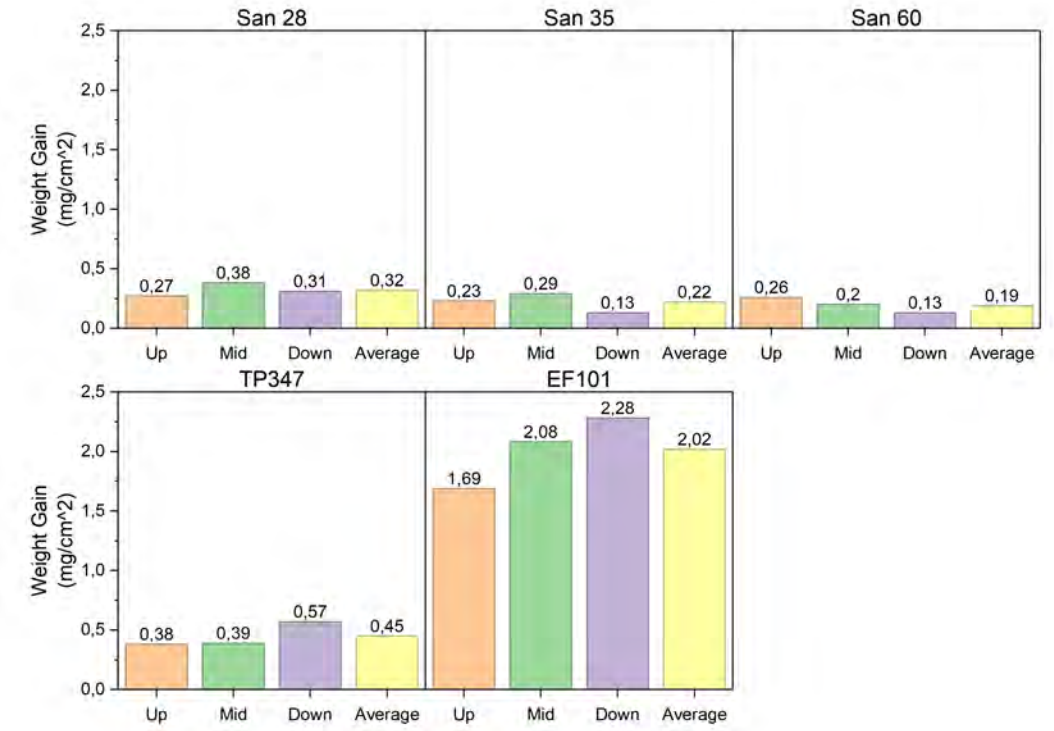

(b) Exposure 2

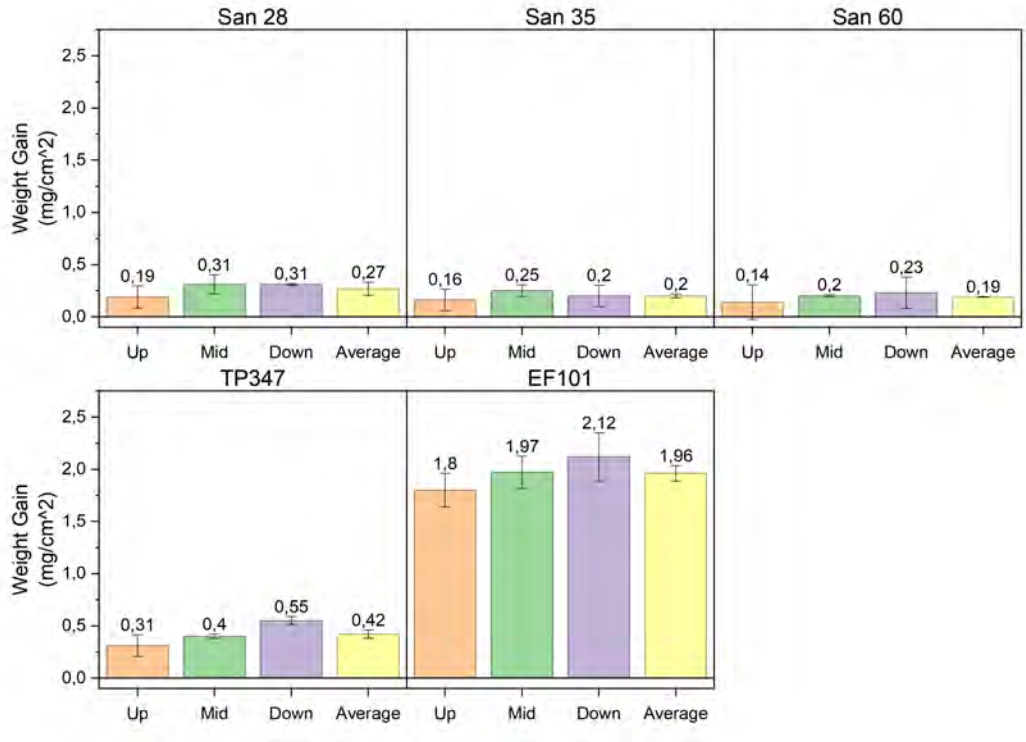

(c) Mean corrected weight gain for samples exposed in Exposure 1 and Exposure 2, with standard deviation, showing upstream, midstream, downstream, and overall average values

Figure 4.4: Weight change measurements corrected for KCl loss for San 28, San 35, San 60, TP347, EF101 and gold samples, exposed to 20% H_2O, a CO_2 flow rate of 950 ml/min, O_2 flow rate of 50 ml/min at 400°C for 168h

Although the true extent of corrosion cannot be determined from 4.3c due to Cr evaporation and loss of KCl, the measured mass gain can be adjusted by accounting for the mass loss of KCl. This adjusted value is referred to as the corrected mass gain. However, it should be noted that this does not represent the true extent of corrosion, as Cr evaporation has not been measured. Nevertheless, it may be considered a close approximation, as Cr evaporation from chromium-containing reaction products is expected to be negligible under the present conditions. K_2CrO_4 at 400°C does not show a measurable vapor pressure, another possible reaction product, $CrO_2(OH)_2$, has a vapor pressure in the range of $4{,}47^{-9}$ bar at this temperature, which is significantly lower than that of KCl. Furthermore, equilibrium calculations using FactSage 8.4 showed that loss of KCl, as observed on the gold samples in Figures 4.3a and 4.3b, may be possible by mechanisms other than spallation. KCl may enter the gas phase in very small amounts with only 10^{-6} moles of salt is calculated as being lost to the gas phase, forming a mole fraction of 5.393×10^{-10}. This may constitute a pathway for KCl loss by it leaving the system in the gas phase. Another pathway is the following reaction:

$$2\,\mathrm{KCl(s)} + \mathrm{H_2O(g)} + \mathrm{CO_2} \longrightarrow 2\,\mathrm{HCl(g)} + \mathrm{K_2CO_3(s)}$$

This reaction forms gaseous HCl from solid KCl, removing heavy Cl atoms and

constituting a mass loss despite the formation of solid K_2CO_3. This reaction is shown to be possible by FactSage calculations, albeit in small amounts, showing a 6.948×10^{-9} mole fraction for HCl in the gas phase and a 7.311×10^{-4} mole fraction for K_2CO_3 in the solid phase. This gives a reduction from KCl constituting the entire solid phase to it making up 99.9 mol% of it. Therefore, loss of KCl from chemical reaction and evaporation is likely negligible and KCl spallation is assumed to be the dominant contributor to the observed mass loss, and the corrected mass gain can be regarded as an approximate indicator for the true extent of corrosion. To obtain the corrected mass gain for each alloy, the weight changes measured up, mid- and downstream for gold are added to the corresponding alloy measurements. The mean corrected weight change for all samples across both exposures is shown in 4.4c.

4.3 Surface and Cross-Sectional Analysis

Table 4.1: Oxide scale thickness measurements.

Alloy	Thickness (µm)	Calculated thickness (µm)
Sanicro 28	0.234	2.748
Sanicro 35	0.051	2.342
Sanicro 60	0.089	2.358
T22	27.981	26.573
TP347 inward	1.808	-
TP347 outward	0.207	-
TP347 total	2.015	4.619
EF101 spalled	28.205	-
EF101 attached	1.058	-
EF101 total	29.263	20.418

Plan view surface SEM characterization of all samples, as seen in Figure 4.5, revealed unreacted KCl remaining on the surface. Notably, Sanicro 28 (Fig. 4.5a) showed a complete KCl coverage, in contrast to a 10% coverage shown in N_2-containing gas [64]. On Sanicro 35, Sanicro 60, and TP347 (Fig. 4.5b, 4.5c, 4.5d), the raw metal surface was visible while otherwise being covered by KCl, similar to the pre-exposure appearance seen in Figure 4.5f. EF101 (Fig. 4.5e) has an appearance comparable to that of T22 (Fig. 4.2a), indicating that both EF101 and T22 experienced more severe corrosion than other samples. Cross-sectional analysis revealed thin oxide scales below the KCl on Sanicro 28, Sanicro 35, Sanicro 60, and TP347 (Fig. 4.6a, 4.6c, 4.6d, 4.6b). EF101 had a thick layer of breakaway corrosion, containing the original metal surface (Fig. 4.6e), as well as an attached layer (Fig. 4.6f). Sanicro 60 scale was detectable by SEM (Fig. 4.6d) but not EDS, but its existence is supported by the weight gain showed in the gravimetric data (Fig. 4.4). All samples, except T22 and EF101, have scale thicknesses significantly lower than the calculated values (Table 4.1), indicating that those samples experienced less corrosion than expected,

while the scale thicknesses for T22 and EF101 are in relatively good agreement with the expected values.

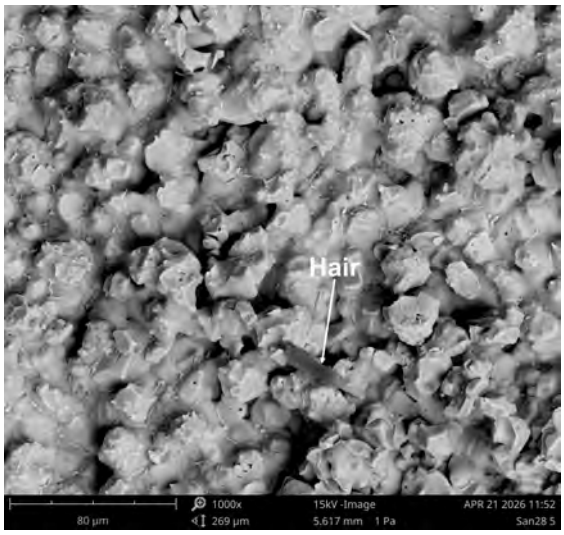

(a) Sanicro 28

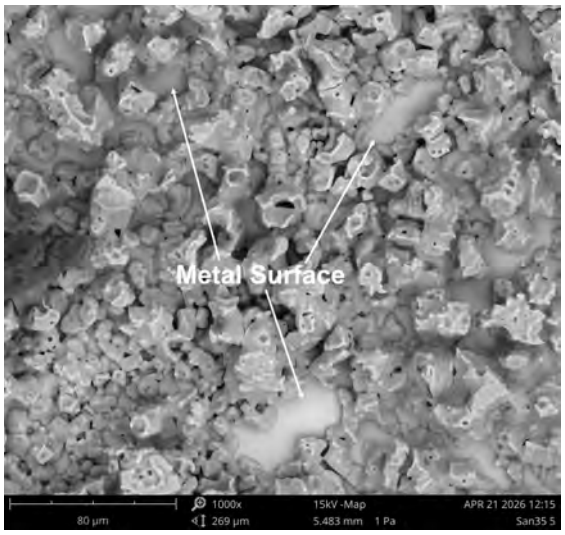

(b) Sanicro 35

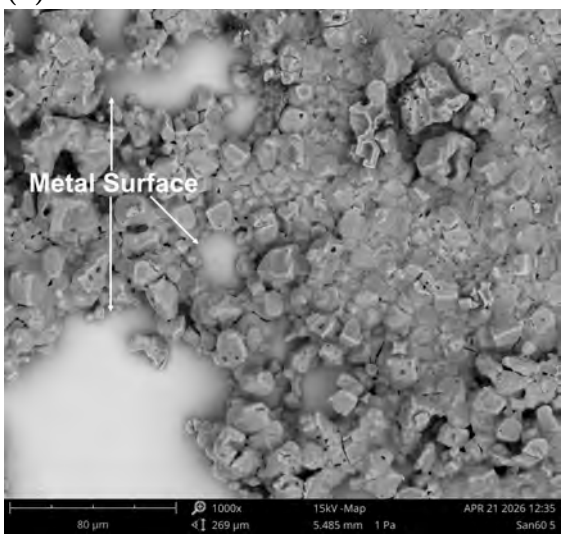

(c) Sanicro 60

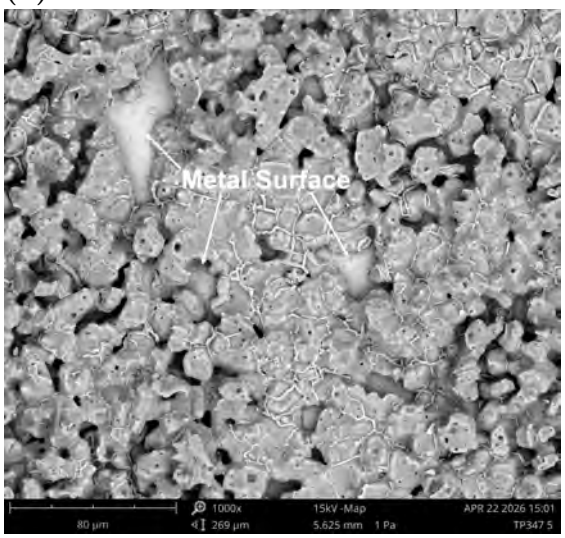

(d) TP347

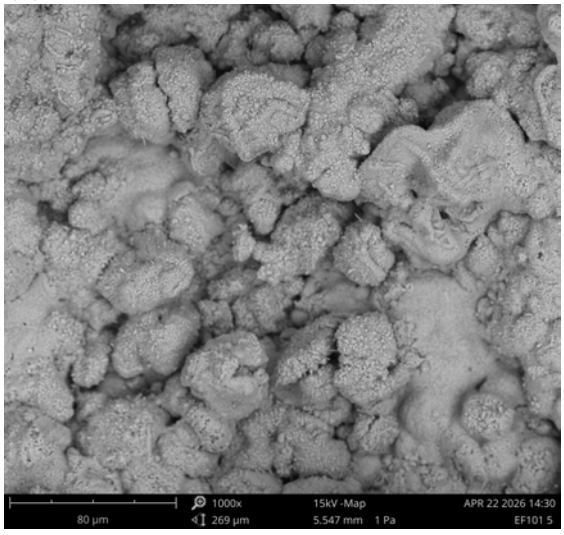

(e) EF101

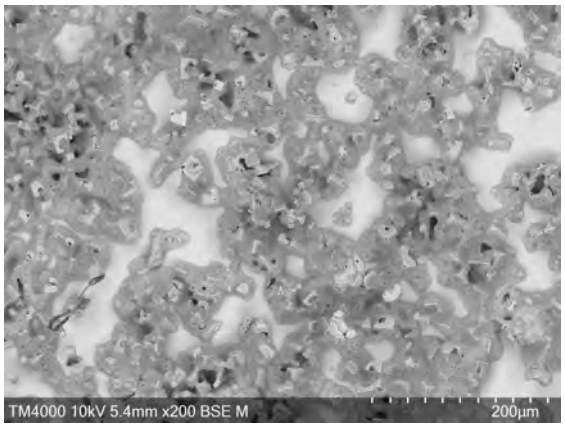

(f) Sample before exposure

Figure 4.5: SEM plan views after 168h exposed to 20% H_2O, a CO_2 flow rate of 950 ml/min, O_2 flow rate of 50 ml/min at 400°C and before exposure

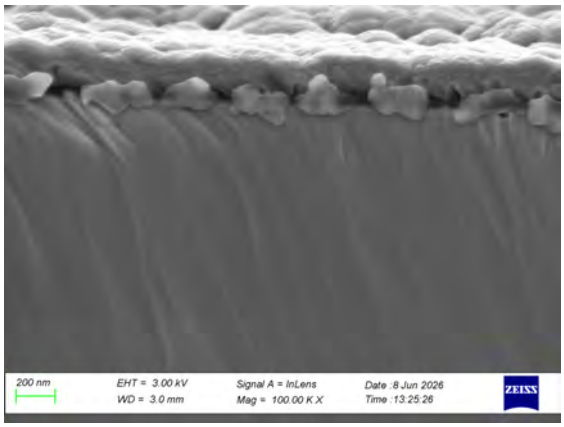

(a) Sanicro 28

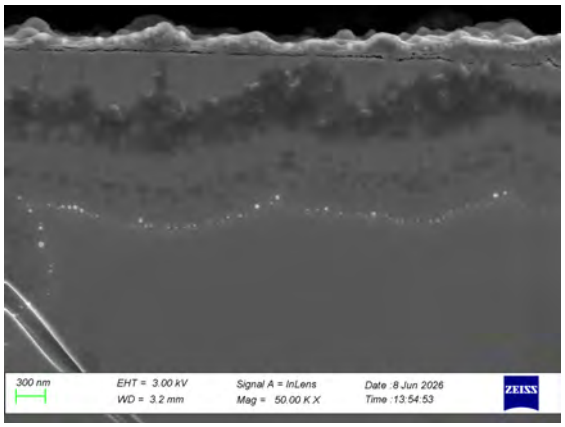

(b) TP347

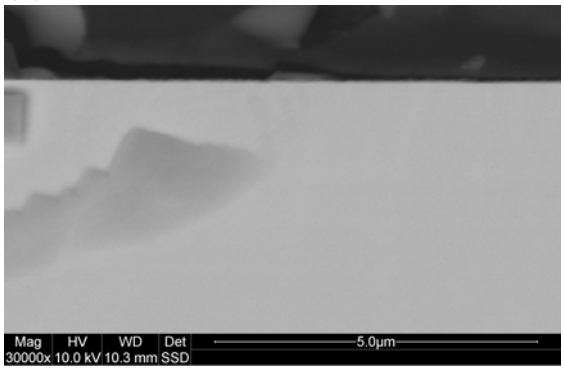

(c) Sanicro 35

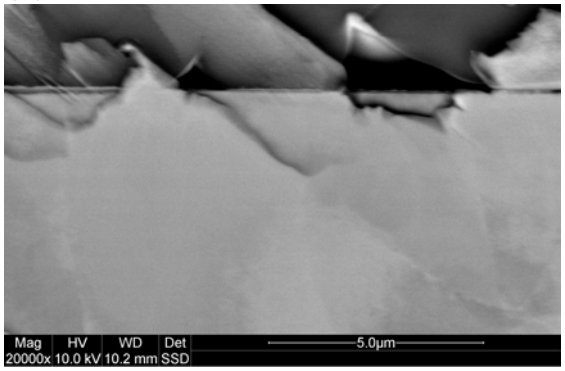

(d) Sanicro 60

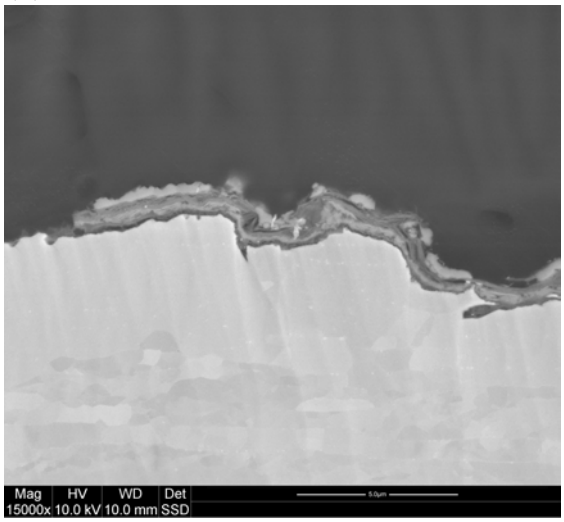

(e) EF101 attached scale

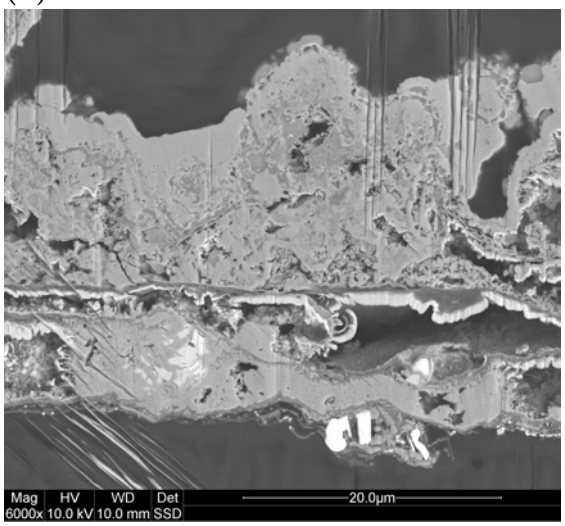

(f) EF101 breakaway scale

Figure 4.6: SEM cross sections after 168h exposed to 20% H_2O, a CO_2 flow rate of 950 ml/min, O_2 flow rate of 50 ml/min at 400°C

4.3.1 Sanicro 28

EDS analysis of Sanicro 28 cross-section showed the formation of a thin oxide scale, as evidenced by the presence of oxygen (Fig. 4.7b), iron (Fig. 4.7c) and chromium (Fig. 4.7d). This indicates the formation of an oxide which can be chromia and/or

a $(Fe,Cr)_3O_4$ spinel, but it has not been possible to identify due to the resolution of the EDS [64]. Chlorine (Fig. 4.7f) and potassium (Fig. 4.7g) are also seen to be present at the scale, indicating that the scale may have grown around KCl particles. It is, however, not possible to rely on EDS for accurate characterization of specific points in the image due to the thin scale and high magnification needed, making the interaction volume too large to accurately determine the atomic makeup at a given point. Instead, EDS can show larger trends in depletion or accumulation of elements on different parts of the image. Accordingly, a greater accumulation of Cl than K is observed along the scale, consistent with the electrochemical mechanism. According to this mechanism, KCl reacts at the surface, e.g., with water and oxygen to form KOH and Cl^- ions, initiating a reaction that runs parallel to the oxide growth [65]. Cl^- then diffuses into the scale along its grain boundaries and, since the diffusion of Cl^- is fast, it will react with Fe at the metal surface, forming $FeCl_2$ [65]. The formation of $FeCl_2$ along the grain boundaries facilitates ion diffusion along the grain boundaries, thus increasing the oxidation rate [65]. This explanation is further supported by the presence of small nodules below the scale of Sanicro 28, seen in Figure 4.6a. Sanicro 35 and Sanicro 60 show similar behavior as indicated by the weight gain (Fig. 4.4), appearance (Fig. 4.5, 4.6), and scale thickness (Table. 4.1).

4.3.2 EF101

Cross-sectional analysis of EF101 shows the formation of a thinner surface oxide scale and a spalled thicker oxide scale (Fig. 4.6f). The EDS analysis of EF101 in Figure 4.8 shows the multilayered oxide scale, as seen in Figure 4.8c an outer Al-rich oxide scale is formed along with the formation of a FeCr-spinel underneath (Fig. 4.8d and Fig. 4.8e) and a thin band of silica at the metal oxide interface (Fig. 4.8f). The presence of Cl within the lower oxide scale (Fig. 4.8g) indicates that chlorine-containing species became mobile during exposure. The corrosivity of alkali chlorides has traditionally been attributed to the active oxidation mechanism, in which molecular Cl_2 gas is assumed to diffuse through the oxide scale and react with the alloying elements, forming volatile metal chlorides which are re-oxidized near the oxide surface at higher oxygen partial pressure, regenerating chlorine-containing species and sustaining the corrosion process [65, 66]. The main criticism of this mechanism is that it requires transport of molecular chlorine species through an oxide scale that simultaneously maintains a significant oxygen potential gradient [65]. Consequently, alternative mechanisms have been proposed to explain the acceleration of corrosion by alkali chlorides. Chlorine-induced corrosion in the presence of KCl has been extensively reported for Fe-based alloys, where chloride species have been shown to accelerate corrosion by changing transport processes within the oxide scale and reducing scale adhesion [65]. Previous work has suggested that chloride ions can migrate through oxide defects and participate in electrochemical transport processes and promote degradation of the protective oxide scale [67]. Chlorine ions may have penetrated the scale through grain boundaries or other oxide defects, facilitating the formation of chloride-containing phases within the scale. Such chloride-containing phases within the oxide scale can change ionic transport processes and reduce scale

protectiveness, consequently contributing to accelerated corrosion and breakaway oxidation. The enrichment of Cl within the Al-rich scale suggests interactions between chloride species and Al-containing phases. Such interactions may reduce the availability of Al for the formation and maintenance of a continuous protective α-alumina scale. Potassium is detected primarily within the spalled oxide scale (Fig. 4.9h), whereas chlorine-enrichment is observed deeper within the lower oxide (Fig. 4.8g). This separation of K and Cl suggests that chloride-containing species were more mobile than potassium-containing species during exposure. This observation is consistent with the proposed electrochemical transport mechanism in which chloride ions diffuse through oxide defects while potassium remains enriched in the outer corrosion product. The spalled oxide scale consists mainly of Fe- and Cr-rich (Fig. 4.9d, 4.9e) oxides, while Si and Al enrichment (Fig. 4.9f, 4.9c) is retained close to the original alloy surface. The transition from an Al-rich scale to Fe- and Cr-rich corrosion products suggests the loss of the primary protection and the onset of breakaway corrosion.

4.3.3 TP347

Cross-sectional EDS investigation of the scale on TP347 shows the presence of oxygen at the surface (Fig. 4.10b), consistent with an oxide scale. Due to the high atom% of Fe (Fig. 4.10i), this is likely Fe_2O_3 and Fe_3O_4. Cross-sectional EDS investigation of TP347 revealed the presence of an oxygen-rich surface layer (Fig. 4.10b), confirming the formation of an oxide scale during exposure. The electron image shows a multilayered oxide scale consisting of a thin inner oxide at the metal/oxide interface enriched in chromium and iron (Fig. 4.10d and Fig. 4.10c), and a thicker outer oxide scale enriched in Fe. Topographical changes close to the metal oxide interface can also be observed indicating possible internal oxidation, forming an outward-growing Fe-rich oxide scale and an inward-growing Fe,Cr-rich spinel beneath the external oxide. In addition to the external scale, an internal oxidation zone is observed more clearly in 4.6b where oxidation extends beneath the oxide/alloy interface. The internal oxidation shows a heterogeneous penetration depth, extending deeper closer to grain boundaries than within grain interiors. This suggests that grain boundaries act as preferential diffusion pathways during oxidation. This may result in local chromium depletion beneath the scale, which limits the alloy's ability to form a protective Cr-rich Fe,Cr spinel thereby facilitating deeper oxidation along the grain boundaries. Additionally, no Cl-enrichment could be identified in the oxide scale, contrary to the San 28 and EF101 samples. The absence of chlorine within the scale might be caused by limitations with the EDS or it can suggest that the corrosion mechanism of TP347 may be governed by a different degradation process compared to the earlier alloys.

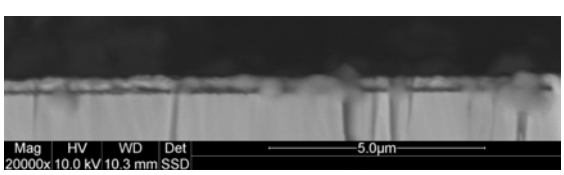

(a) Electron image

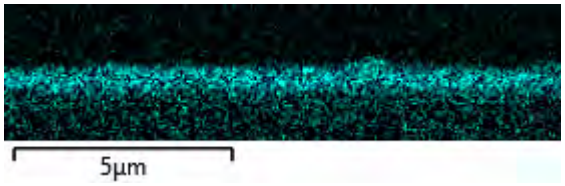

(b) Oxygen

(c) Iron

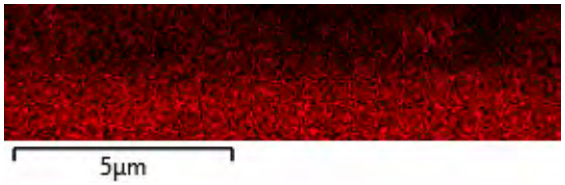

(d) Chromium

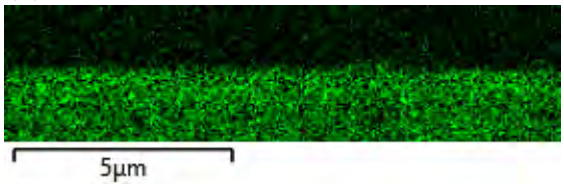

(e) Nickel

(f) Chlorine

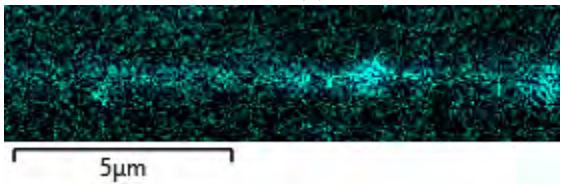

(g) Potassium

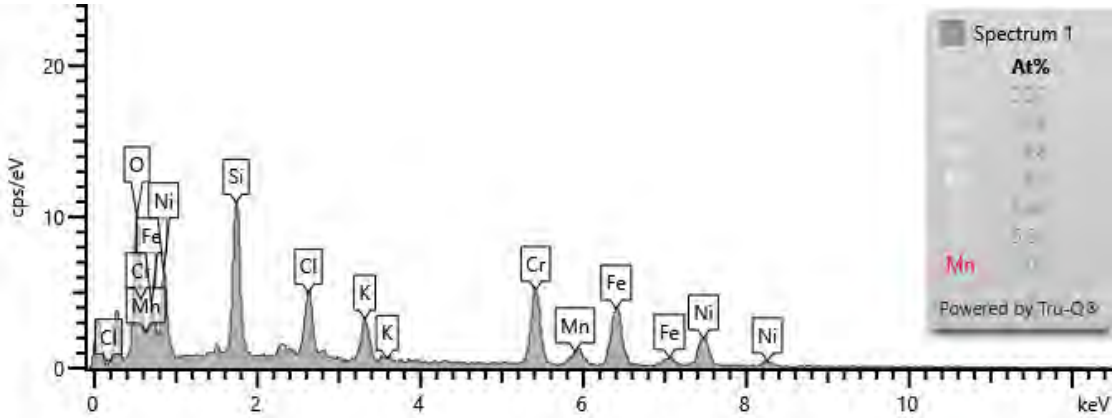

(h) Scale Composition

Figure 4.7: BSE-SEM cross section and EDS mapping of Sanicro 28 after 168h exposed to 20% H_2O, a CO_2 flow rate of 950 ml/min, O_2 flow rate of 50 ml/min at 400°C

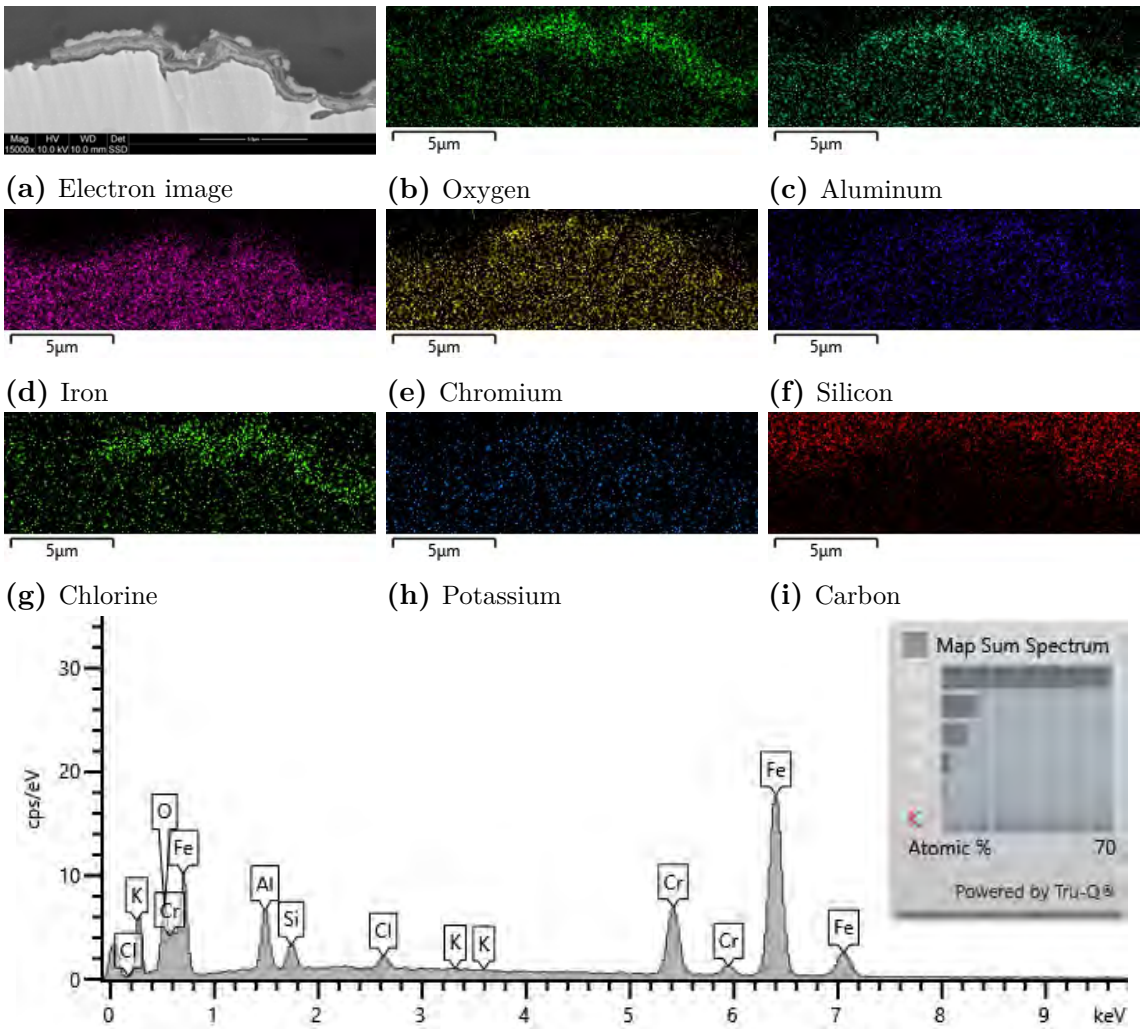

(a) Electron image **(b)** Oxygen **(c)** Aluminum

(d) Iron **(e)** Chromium **(f)** Silicon

(g) Chlorine **(h)** Potassium **(i)** Carbon

(j) Scale Composition

Figure 4.8: BSE-SEM cross section and EDS mapping of EF101 attached scale after 168h exposed to 20% H_2O, a CO_2 flow rate of 950 ml/min, O_2 flow rate of 50 ml/min at 400°C

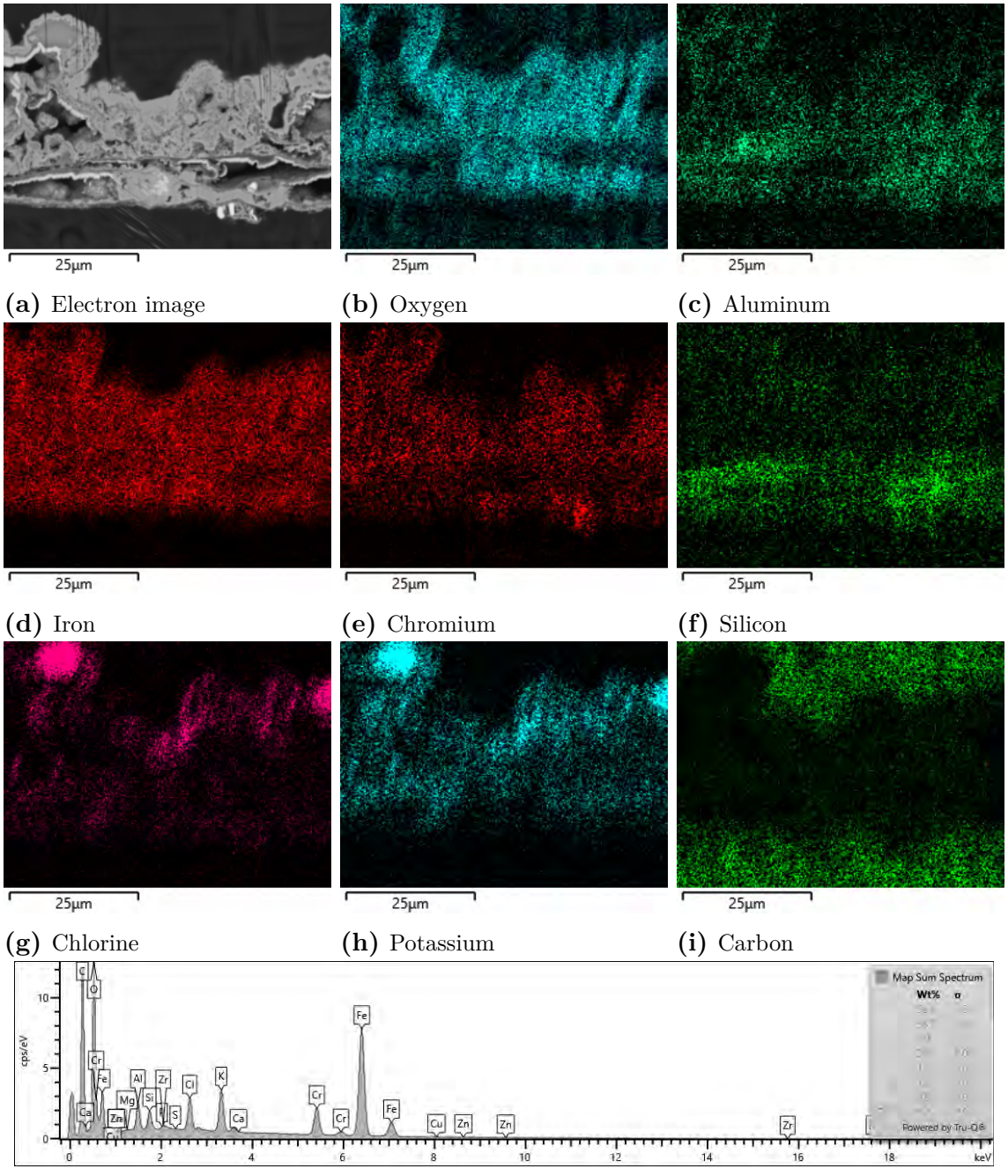

(a) Electron image **(b)** Oxygen **(c)** Aluminum

(d) Iron **(e)** Chromium **(f)** Silicon

(g) Chlorine **(h)** Potassium **(i)** Carbon

(j) Scale Composition

Figure 4.9: BSE-SEM cross section and EDS mapping of EF101 spalled scale after 168h exposed to 20% H_2O, a CO_2 flow rate of 950 ml/min, O_2 flow rate of 50 ml/min at 400°C

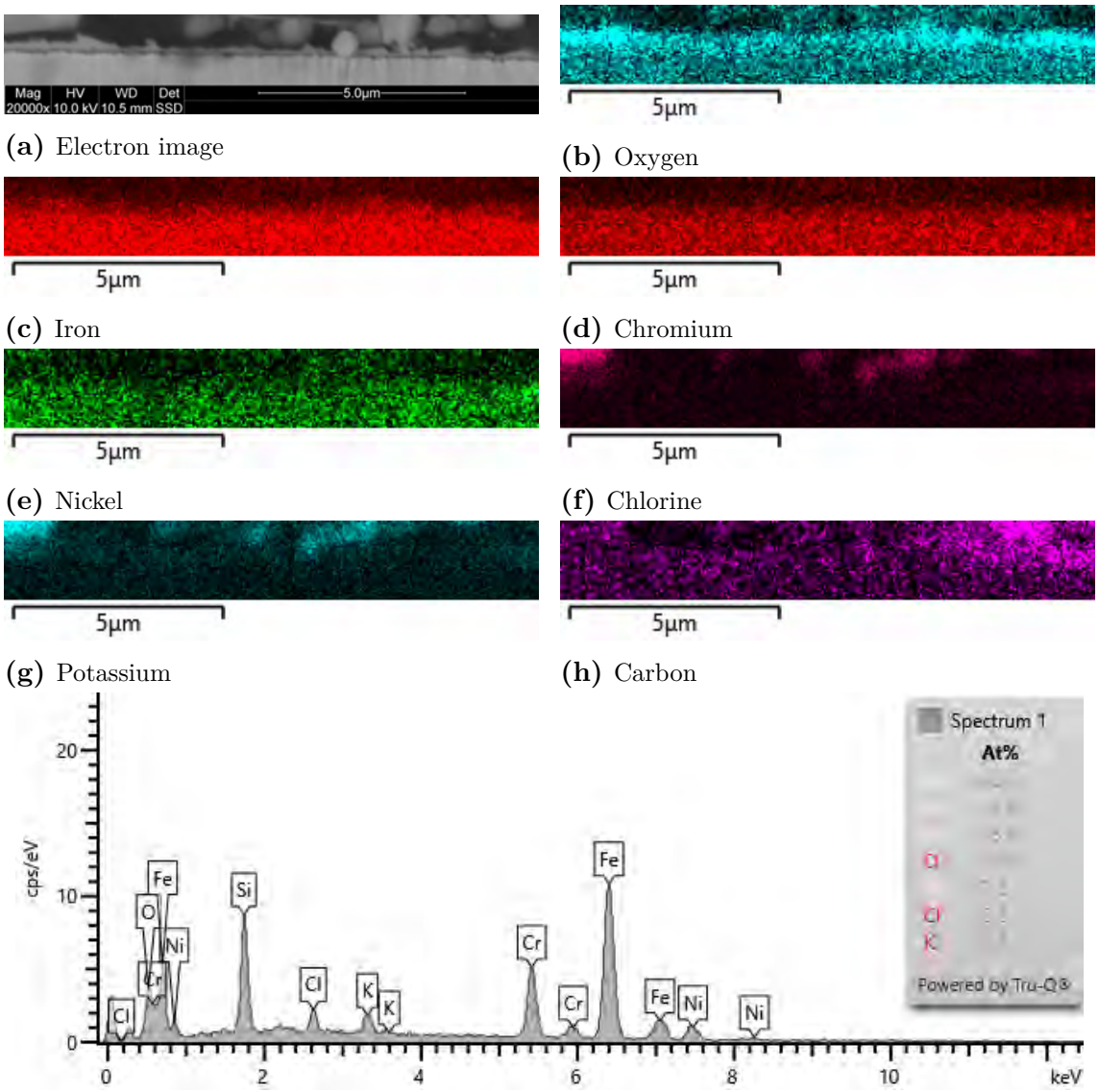

(a) Electron image

(b) Oxygen

(c) Iron

(d) Chromium

(e) Nickel

(f) Chlorine

(g) Potassium

(h) Carbon

(i) Scale Composition

Figure 4.10: BSE-SEM cross section and EDS mapping of TP347 after 168h exposed to 20% H_2O, a CO_2 flow rate of 950 ml/min, O_2 flow rate of 50 ml/min at 400°C

5
Conclusion

This thesis has developed and tested an exposure methodology for laboratory testing of corrosion in simulated fuel reactor environments. However, the robustness of this method is unclear due to inconclusive gravimetric data. Also, candidate materials for use as superheater materials in the fuel side reactor of chemical looping combustion plants have been investigated. Six materials were exposed in 5% O_2 + 20% H_2O + CO_2 bal gas at 400°C for 168 h to investigate their corrosion properties in a high-water, nitrogen-free atmosphere, simulating the FR side of a CLC system. KCl was deposited on each sample to investigate the effects of alkali chlorides, typical of waste-fired boilers. The present study found that Sanicro 28 experienced little corrosion, with low weight gain and thin oxide formation. Furthermore, Sanicro 35 and Sanicro 60 exhibited similarly high corrosion resistance under the present conditions. EF101 experienced corrosion to an extent similar of the low-alloy steel T22 but with less severe spallation. The poorer performance of EF101 is attributed to the inability to establish and maintain a continuous protective Al-rich oxide scale and the subsequent formation of less protective Fe-rich and Cr-rich corrosion products, resulting in breakaway oxidation. It has thus been shown that Sanicro 28, Sanicro 35, Sanicro 60, and TP347 show great promise as superheater materials, with less frequent maintenance being needed compared to T22. EF101 has displayed little benefit over the more inexpensive T22. From an economic investment perspective, TP347 is the preferred alternative to low-alloy steels, such as T22, due to its improved corrosion properties and with it having the lowest nickel-content out of the other alternatives investigated, its cost is also lower.

6
Future Work

While this thesis provides valuable information on the corrosion behavior of the investigated alloys, the results show that additional research is required. Future studies should therefore focus on extending the exposure duration which would provide information on the long term stability of the formed oxide scales, along with the progression of breakaway corrosion. By extending exposures, determination of whether the observed oxidation and breakaway mechanism continue or if protective scales are re-established or healing layers eventually formed. Future studies should also include investigation of alloy performance under dual-atmosphere conditions to better simulate real world application environments. The exposure to both combustion gas and steam may influence the oxide growth, transport processes, material strength, and corrosion resistance differently than single atmosphere exposures.
Surface coating could also be of interest, as a means of reducing chloride diffusion which could improve scale stability. This could help determine whether surface coatings are capable of suppressing chlorine degradation mechanisms like the electrochemical transport mechanism observed in this thesis. Since deposits affect the high-temperature corrosion of superheater materials, the use of anti-fouling coatings could be used in environments representative of CLC systems.
Although laboratory exposures do provide controlled conditions and reproducibility, field testing is required to assess the true performance of an alloy under the complex and varying conditions encountered in operating CLC plants. This would provide validation for observations made in this thesis.

Bibliography

[1] IEA. *Global electricity demand is set to grow strongly to 2030, underscoring need for investments in grids and flexibility*. Feb. 2026. URL: https://www.iea.org/news/global-electricity-demand-is-set-to-grow-strongly-to-2030-underscoring-need-for-investments-in-grids-and-flexibility.

[2] Tomasz Czakiert et al. "Chemical Looping Combustion: A Brief Overview". In: *Energies* 15.4 (2022). ISSN: 1996-1073. DOI: 10.3390/en15041563. URL: https://www.mdpi.com/1996-1073/15/4/1563.

[3] *World Corrosion Awareness Day 2025 Media Kit*. World Corrosion Organization, Apr. 2025. URL: https://corrosion.org/World+Corrosion+Awareness+Day+2025+Media+Kit-p-2750/_/World%20Corrosion%20Awareness%20Day%202025%20Media%20Kit.pdf.

[4] Mamoru Ozawa. "2 - Introduction to boilers". In: *Advances in Power Boilers*. Ed. by Mamoru Ozawa and Hitoshi Asano. Vol. 2. JSME Series in Thermal and Nuclear Power Generation. Elsevier, 2021, pp. 57–106. ISBN: 978-0-12-820360-6. DOI: https://doi.org/10.1016/B978-0-12-820360-6.00002-3. URL: https://www.sciencedirect.com/science/article/pii/B9780128203606000023.

[5] Esa Kari Vakkilainen. "10 - Fluidized Bed Boilers for Biomass". In: *Steam Generation from Biomass*. Ed. by Esa Kari Vakkilainen. Butterworth-Heinemann, 2017, pp. 211–236. ISBN: 978-0-12-804389-9. DOI: https://doi.org/10.1016/B978-0-12-804389-9.00010-1. URL: https://www.sciencedirect.com/science/article/pii/B9780128043899000101.

[6] Luke Makarichi, Warangkana Jutidamrongphan, and Kua-anan Techato. "The evolution of waste-to-energy incineration: A review". In: *Renewable and Sustainable Energy Reviews* 91 (2018), pp. 812–821. ISSN: 1364-0321. DOI: https://doi.org/10.1016/j.rser.2018.04.088. URL: https://www.sciencedirect.com/science/article/pii/S1364032118302855.

[7] Chhotu Ram, Amit Kumar, and Pushpa Rani. "Municipal solid waste management: A review of waste to energy (WtE) approaches". In: *BioResources* (2021). URL: https://api.semanticscholar.org/CorpusID:236749599.

[8] Efstratios N. Kalogirou. *Waste-to-Energy Technologies and Global Applications*. CRC Press, Dec. 2024. URL: https://www.taylorfrancis.com/books/edit/10.1201/9781003567547/waste-energy-technologies-global-applications-efstratios-kalogirou.

[9] Paul H Brunner and Leo S Morf. "Waste to energy, indispensable cornerstone for circular economy: A mini-review". In: *SageJournals* (2024). URL: https://journals.sagepub.com/doi/10.1177/0734242X241227376.

[10] Vattenfall. *Transforming waste into energy*. URL: https://group.vattenfall.com/our-operations/our-energy-sources/waste.

[11] ESWET. *A look inside a Waste-to-Energy Plant: components and technologies*. Mar. 2024. URL: https://eswet.eu/a-look-inside-a-waste-to-energy-plant-components-and-technologies/.

[12] George Y. Lai. *High-Temperature Corrosion and Materials Applications*. ASM Technical Books, 2007. URL: https://www.docenti.unina.it/webdocenti-be/allegati/materiale-didattico/434937.

[13] Farzad Moradian et al. "Co-Combustion of Animal Waste in a Commercial Waste-to-Energy BFB Boiler". In: *Energies* 6.12 (2013), pp. 6170–6187. ISSN: 1996-1073. DOI: 10.3390/en6126170. URL: https://www.mdpi.com/1996-1073/6/12/6170.

[14] Farzad Moradian et al. "Examples of Full Scale Tests on BFB Waste-to-Energy Boilers". In: Available via DiVA Portal. 2012. URL: https://www.diva-portal.org/smash/get/diva2:887571/FULLTEXT01.pdf.

[15] Heat Management. *How to master the fouling challenges with biofuel- and waste-to-energy boilers*. Dec. 2021. URL: https://heatmanage.com/news/how-to-master-the-fouling-challenges-with-biofuel-and-waste-to-energy-boilers/.

[16] Kritkasem Khantisopon et al. "High Temperature Corrosion Resistant and Anti-slagging Coatings for Boilers: A Review". In: *High Temperature Corrosion of Materials* 101 (2024), pp. 1–55. DOI: https://doi.org/10.1007/s11085-024-10251-0. URL: https://link.springer.com/article/10.1007/s11085-024-10251-0.

[17] Shreekant B. Malvadkar, Sarah Forbes, and Gilbert V. McGurl. "Coal Resources, Formation of". In: *Encyclopedia of Energy*. Ed. by Cutler J. Cleveland. New York: Elsevier, 2004, pp. 529–550. ISBN: 978-0-12-176480-7. DOI: https://doi.org/10.1016/B0-12-176480-X/00281-3. URL: https://www.sciencedirect.com/science/article/pii/B012176480X002813.

[18] SINTEF projects. *LOUISE – Low-cost CO2 capture by chemical looping combustion of waste-derived fuels*. URL: https://www.sintef.no/en/projects/2021/louise-low-cost-co2-capture-by-chemical-looping-combustion-of-waste-derived-fuels/.

[19] Francis Chinweuba Eboh, Bengt-Åke Andersson, and Tobias Richards. "Economic evaluation of improvements in a waste-to-energy combined heat and power plant". In: *Waste Management* 100 (2019), pp. 75–83. ISSN: 0956-053X. DOI: https://doi.org/10.1016/j.wasman.2019.09.008. URL: https://www.sciencedirect.com/science/article/pii/S0956053X19305859.

[20] Rodolfo L. B. A. Medeiros Rebecca A. B. Nascimento et al. "Mn/MgAl2O4 oxygen carriers for chemical looping combustion using coal: influence of the thermal treatment on the structure and reactivity". In: *Journal of Thermal Analysis and Calorimetry* (2020), pp. 2673–2685. DOI: https://doi.org/10.

1007/s10973-019-09014-w. URL: https://link.springer.com/article/10.1007/s10973-019-09014-w#citeas.

[21] Antonio Coppola and Fabrizio Scala. "Chemical Looping for Combustion of Solid Biomass: A Review". In: *Energy & Fuels* (2021), pp. 19248–19265. DOI: doi:10.1021/acs.energyfuels.1c02600. URL: https://pubs.acs.org/doi/10.1021/acs.energyfuels.1c02600#:~:text=looping%20combustion%20(CLC)%20is%20a%20promising%20CO2,aiming%20to%20avoid%20nitrogen%20in%20combustion%20exhaust..

[22] Jochen Ströhle. "Chemical Looping Combustion of Waste-Opportunities and Challenges". In: *Energy & Fuels* 37 (2023), pp. 1465–1471. ISSN: 0887-0624. DOI: https://doi.org/10.1021/acs.energyfuels.2c04297. URL: https://pubs.acs.org/doi/10.1021/acs.energyfuels.2c04297.

[23] B. O. Oboirien & H. Leion Z. T. Yaqub. "Chemical looping combustion (CLC) of municipal solid waste (MSW)". In: *Journal of Material Cycles and Waste Management* 25 (2023), pp. 1900–1920. DOI: https://doi.org/10.1007/s10163-023-01674-z. URL: https://link.springer.com/article/10.1007/s10163-023-01674-z.

[24] Xi Chen et al. "Engineering design and numerical design for chemical looping combustion reactor: A review". In: *Energy Reviews* 3.3 (2024), p. 100100. ISSN: 2772-9702. DOI: https://doi.org/10.1016/j.enrev.2024.100100. URL: https://www.sciencedirect.com/science/article/pii/S2772970224000336.

[25] B. Erlach, M. Schmidt, and G. Tsatsaronis. "Comparison of carbon capture IGCC with pre-combustion decarbonisation and with chemical-looping combustion". In: *Energy* 36.6 (2011). ECOS 2009, pp. 3804–3815. ISSN: 0360-5442. DOI: https://doi.org/10.1016/j.energy.2010.08.038. URL: https://www.sciencedirect.com/science/article/pii/S0360544210004743.

[26] Hayder A. Alalwan and Alaa H. Alminshid. "CO2 capturing methods: Chemical looping combustion (CLC) as a promising technique". In: *Science of The Total Environment* 788 (2021), p. 147850. ISSN: 0048-9697. DOI: https://doi.org/10.1016/j.scitotenv.2021.147850. URL: https://www.sciencedirect.com/science/article/pii/S0048969721029211.

[27] Masoud Seyyedattar and Sohrab Zendehboudi. "Carbon capture and storage: A comprehensive review on current trends, techniques, and future prospects in North America". In: *Fuel* 407 (2026), p. 137276. ISSN: 0016-2361. DOI: https://doi.org/10.1016/j.fuel.2025.137276. URL: https://www.sciencedirect.com/science/article/pii/S0016236125030017.

[28] Haibo Zhao et al. *Chemical looping combustion: Advantages, disadvantages, opportunities and challenges*. 2025. DOI: 10.59717/j.xinn-energy.2025.100118. URL: https://www.the-innovation.org/energy/article/id/68da2362eaedd90f4121f5c2.

[29] Tobias Mattisson, Anders Lyngfelt, and Henrik Leion. "Chemical-looping with oxygen uncoupling for combustion of solid fuels". In: *International Journal of Greenhouse Gas Control* 3.1 (2009), pp. 11–19. ISSN: 1750-5836. DOI: https://doi.org/10.1016/j.ijggc.2008.06.002. URL: https://www.sciencedirect.com/science/article/pii/S1750583608000510.

[30] J. Adánez et al. “Chemical looping combustion of solid fuels”. In: *Progress in Energy and Combustion Science* 65 (2018), pp. 6–66. ISSN: 0360-1285. DOI: https://doi.org/10.1016/j.pecs.2017.07.005. URL: https://www.sciencedirect.com/science/article/pii/S0360128517300199.

[31] Hampus Lindmark et al. “Corrosivity of KOH(g) towards superheater materials in a simulated air reactor environment for chemical looping combustion of biomass”. In: *Fuel* 381 (2025), p. 133178. ISSN: 0016-2361. DOI: https://doi.org/10.1016/j.fuel.2024.133178. URL: https://www.sciencedirect.com/science/article/pii/S0016236124023275.

[32] Haibo Zhao et al. “Development of tailor-made oxygen carriers and reactors for chemical looping processes at Huazhong University of Science & Technology”. In: *International Journal of Greenhouse Gas Control* 93 (2020), p. 102898. ISSN: 1750-5836. DOI: https://doi.org/10.1016/j.ijggc.2019.102898. URL: https://www.sciencedirect.com/science/article/pii/S1750583619304748.

[33] C. Linderholm and A. Lyngfelt. “14 - Chemical-looping combustion of solid fuels”. In: *Calcium and Chemical Looping Technology for Power Generation and Carbon Dioxide (CO2) Capture*. Ed. by Paul Fennell and Ben Anthony. Woodhead Publishing Series in Energy. Woodhead Publishing, 2015, pp. 299–326. ISBN: 978-0-85709-243-4. DOI: https://doi.org/10.1016/B978-0-85709-243-4.00014-8. URL: https://www.sciencedirect.com/science/article/pii/B9780857092434000148.

[34] Raghvendra Kumar Gupta et al. “Reactor design and process optimization in chemical looping combustion: Insights into fuel types, oxygen carriers, and process design”. In: *Journal of Environmental Chemical Engineering* 13.3 (2025), p. 116561. ISSN: 2213-3437. DOI: https://doi.org/10.1016/j.jece.2025.116561. URL: https://www.sciencedirect.com/science/article/pii/S2213343725012576.

[35] Tao Song and Laihong Shen. “Review of reactor for chemical looping combustion of solid fuels”. In: *International Journal of Greenhouse Gas Control* 76 (2018), pp. 92–110. ISSN: 1750-5836. DOI: https://doi.org/10.1016/j.ijggc.2018.06.004. URL: https://www.sciencedirect.com/science/article/pii/S175058361730837X.

[36] Orlando Palone et al. “Decarbonizing power and fuels production by chemical looping processes: Systematic review and future perspectives”. In: *Applied Thermal Engineering* 254 (2024), p. 123844. ISSN: 1359-4311. DOI: https://doi.org/10.1016/j.applthermaleng.2024.123844. URL: https://www.sciencedirect.com/science/article/pii/S1359431124015126.

[37] Juan Adanez et al. “Progress in Chemical-Looping Combustion and Reforming technologies”. In: *Progress in Energy and Combustion Science* 38.2 (2012), pp. 215–282. ISSN: 0360-1285. DOI: https://doi.org/10.1016/j.pecs.2011.09.001. URL: https://www.sciencedirect.com/science/article/pii/S0360128511000505.

[38] Xi Chen and Haibo Zhao. “A self-consistent design method of the autothermal dual circulating fluidized bed reactor for in-situ gasification chemical looping combustion of coal”. In: *Carbon Capture Science & Technology* 13 (2024), p. 100292. ISSN: 2772-6568. DOI: https://doi.org/10.1016/j.ccst.2024.

100292. URL: https://www.sciencedirect.com/science/article/pii/S2772656824001040.

[39] Ashish Soni et al. "Waste-to-energy technologies: a sustainable pathway for resource recovery and materials management". In: *Mater. Adv.* 6 (14 2025), pp. 4598–4622. DOI: 10.1039/D5MA00449G. URL: http://dx.doi.org/10.1039/D5MA00449G.

[40] A. Lyngfelt. "11 - Oxygen carriers for chemical-looping combustion". In: *Calcium and Chemical Looping Technology for Power Generation and Carbon Dioxide (CO2) Capture*. Ed. by Paul Fennell and Ben Anthony. Woodhead Publishing Series in Energy. Woodhead Publishing, 2015, pp. 221–254. ISBN: 978-0-85709-243-4. DOI: https://doi.org/10.1016/B978-0-85709-243-4.00011-2. URL: https://www.sciencedirect.com/science/article/pii/B9780857092434000112.

[41] Ivan Gogolev et al. "Chemical-looping combustion in a 100kW unit using a mixture of synthetic and natural oxygen carriers – Operational results and fate of biomass fuel alkali". In: *International Journal of Greenhouse Gas Control* 88 (2019), pp. 371–382. ISSN: 1750-5836. DOI: https://doi.org/10.1016/j.ijggc.2019.06.020. URL: https://www.sciencedirect.com/science/article/pii/S1750583619301173.

[42] Jan-Erik Eriksson et al. "Corrosion of Heat-Transfer materials Induced by KCl, HCl, and O2 Under Chemical-Looping Conditions". In: *High Temperature Corrosion of Materials* 101 (2024/12/01), pp. 123–141. ISSN: 2731-8400. DOI: https://doi.org/10.1007/s11085-024-10250-1. URL: https://link.springer.com/article/10.1007/s11085-024-10250-1#citeas.

[43] Vicent Ssenteza et al. "High-Temperature Corrosion Behavior of Superheater Materials at 600 °C: Insights from Laboratory and Field Exposures". In: *Energy & Fuels* 39 (2025/01/09), pp. 819–827. ISSN: 0887-0624. DOI: https://doi.org/10.1021/acs.energyfuels.4c04806. URL: https://pubs.acs.org/doi/pdf/10.1021/acs.energyfuels.4c04806?ref=article_openPDF.

[44] Michael J Schofield. "33 - Corrosion". In: *Plant Engineer's Reference Book (Second Edition)*. Ed. by Dennis A. Snow. Second Edition. Oxford: Butterworth-Heinemann, 2002, pp. 33-1-33–25. ISBN: 978-0-7506-4452-5. DOI: https://doi.org/10.1016/B978-075064452-5/50088-2. URL: https://www.sciencedirect.com/science/article/pii/B9780750644525500882.

[45] E. McCafferty. *Introduction to Corrosion Science*. Springer, 2010.

[46] Hampus Lindmark, Torbjörn Jonsson, and Jesper Liske. "A time-resolved study of PbCl2-induced corrosion of low-alloyed steel in the presence of water vapour at 400 °C". In: *Corrosion Science* 229 (2024), p. 111843. ISSN: 0010-938X. DOI: https://doi.org/10.1016/j.corsci.2024.111843. URL: https://www.sciencedirect.com/science/article/pii/S0010938X24000271.

[47] Mathias C. Galetz Clara Schlereth. "Effect of Total Pressure and Furnace Tube Material on the Oxidation of T22 in Humidified Air". In: *Oxidation of Metals* (2021). DOI: https://doi.org/10.1007/s11085-021-10036-9. URL: https://link.springer.com/article/10.1007/s11085-021-10036-9#citeas.

[48] A. Persdotter et al. "Oxidation of Fe-2.25Cr-1Mo in presence of KCl(s) at 400 °C – Crack formation and its influence on oxidation kinetics". In: *Corrosion*

Science 163 (2020), p. 108234. ISSN: 0010-938X. DOI: https://doi.org/10.1016/j.corsci.2019.108234. URL: https://www.sciencedirect.com/science/article/pii/S0010938X19302288.

[49] S. Karlsson et al. "Alkali Induced High Temperature Corrosion of Stainless Steel: The Influence of NaCl, KCl and $CaCl_2$". In: *Oxidation of Metals* (2012). DOI: https://doi.org/10.1007/s11085-012-9293-7. URL: https://link.springer.com/article/10.1007/s11085-012-9293-7#citeas.

[50] M.A Uusitalo, P.M.J Vuoristo, and T.A Mäntylä. "High temperature corrosion of coatings and boiler steels below chlorine-containing salt deposits". In: *Corrosion Science* 46.6 (2004), pp. 1311–1331. ISSN: 0010-938X. DOI: https://doi.org/10.1016/j.corsci.2003.09.026. URL: https://www.sciencedirect.com/science/article/pii/S0010938X03002622.

[51] M. Sánchez Pastén and M. Spiegel. "High temperature corrosion of metallic materials in simulated waste incineration environments at 300-600°C". In: *Materials and Corrosion* (2006). DOI: https://doi.org/10.1002%2Fmaco.200503909. URL: https://onlinelibrary.wiley.com/doi/10.1002/maco.200503909.

[52] Nidhi Raval et al. "Chapter 10 - Importance of Physicochemical Characterization of Nanoparticles in Pharmaceutical Product Development". In: *Basic Fundamentals of Drug Delivery*. Ed. by Rakesh K. Tekade. Advances in Pharmaceutical Product Development and Research. Academic Press, 2019, pp. 369–400. ISBN: 978-0-12-817909-3. DOI: https://doi.org/10.1016/B978-0-12-817909-3.00010-8. URL: https://www.sciencedirect.com/science/article/pii/B9780128179093000108.

[53] Leica Microsystems. *Ion Beam Milling Guide: Enhancing Surface Quality for High-Resolution Imaging and Analysis*. URL: https://www.leica-microsystems.com/science-lab/life-science/ion-beam-milling-guide-enhancing-surface-quality-for-high-resolution-imaging-and-analysis/.

[54] N.G. Chew and A.G. Cullis. "The preparation of transmission electron microscope specimens from compound semiconductors by ion milling". In: *Ultramicroscopy* 23.2 (1987), pp. 175–198. ISSN: 0304-3991. DOI: https://doi.org/10.1016/0304-3991(87)90163-X. URL: https://www.sciencedirect.com/science/article/pii/030439918790163X.

[55] Nils Timmermans et al. "Process optimization of broad ion beam milling for preparation of coating cross-sections". In: *Ultramicroscopy* 255 (2024), p. 113858. ISSN: 0304-3991. DOI: https://doi.org/10.1016/j.ultramic.2023.113858. URL: https://www.sciencedirect.com/science/article/pii/S0304399123001754.

[56] Pawel Nowakowski et al. "Developments in Broad Ion Beam Milling Sample Preparation Instrumentation for Microscopy and Microanalysis Applications". In: *Microscopy and Microanalysis* 29 (2023), pp. 2075–2076. DOI: https://doi.org/10.1093/micmic/ozad067.1074. URL: https://academic.oup.com/mam/article/29/Supplement_1/2075/7228155.

[57] Alleima. *Sanicro® 35 Tube and pipe, seamless*. 2026. URL: https://www.alleima.com/en/technical-center/material-datasheets/tube-and-pipe-seamless/sanicro-35/.

[58] Alleima. *Sanicro® 28 Tube and pipe, seamless*. 2026. URL: https://www.alleima.com/en/technical-center/material-datasheets/tube-and-pipe-seamless/sanicro-28/.

[59] Sandvik Materials Technology. *Sanicro 60*. 2026. URL: https://keevitus.ee/media/attachment/1_sanicro-60.pdf.

[60] Alleima. *Alleima® 6R44 Tube and pipe, seamless*. 2026. URL: https://www.alleima.com/en/technical-center/material-datasheets/tube-and-pipe-seamless/alleima-6r44/.

[61] Kahtan Al-Khazraji, Ahmed Moosa, and Abbas Husssein. "Oxidation Properties of Steel-T22 Alloy Coated by Simultaneous Ge-Doped Chromizing-Siliconizing Process". In: *Eng.& Tech.Journal,Vol.27,No.B,2009* 27 (Jan. 2009). DOI: 10.30684/etj.29.6.11.

[62] Imran Hanif et al. "High-temperature corrosion of weld overlay coating/bulk FeCrAl exposed in O2 + H2O + KCl(s) at 600°C – A microstructural investigation". In: *Journal of Materials Research and Technology* 25 (2023), pp. 7008–7023. ISSN: 2238-7854. DOI: https://doi.org/10.1016/j.jmrt.2023.07.073. URL: https://www.sciencedirect.com/science/article/pii/S2238785423016009.

[63] A. Chyrkin, J. Froitzheim, and W. J. Quadakkers. "Transition from Internal to External Oxidation in Binary Fe–Cr Alloys Around 900 °C". In: *High Temperature Corrosion of Materials* 102.1 (2024), p. 3. ISSN: 2731-8400. DOI: 10.1007/s11085-024-10322-2. URL: https://doi.org/10.1007/s11085-024-10322-2.

[64] J. Phother-Simon et al. "High-Temperature corrosion of P91/T91, 304L, Sanicro 28 and Inconel 625 exposed at 600°C under continuous KCl deposition". In: *Fuel* 357 (2024), p. 130012. ISSN: 0016-2361. DOI: https://doi.org/10.1016/j.fuel.2023.130012. URL: https://www.sciencedirect.com/science/article/pii/S0016236123026261.

[65] N. Folkeson et al. "The influence of small amounts of KCl(s) on the high temperature corrosion of a Fe-2.25Cr-1Mo steel at 400 and 500°C". In: *Materials and Corrosion* 62.7 (2011), pp. 606–615. DOI: https://doi.org/10.1002/maco.201005942. eprint: https://onlinelibrary.wiley.com/doi/pdf/10.1002/maco.201005942. URL: https://onlinelibrary.wiley.com/doi/abs/10.1002/maco.201005942.

[66] Yuchen Cai et al. "Corrosion behaviour of Fe-based austenitic and Ni-based alloys in Wet CO2 gas with and without chloride deposits at 650 C". In: *Corrosion Science* 210 (2023), p. 110822. DOI: 10.1016/j.corsci.2022.110822.

[67] J. Eklund et al. "The long-term corrosion behavior of FeCrAl(Si) alloys after breakaway oxidation at 600°C". In: *Corrosion Science* 217 (2023), p. 111155. ISSN: 0010-938X. DOI: https://doi.org/10.1016/j.corsci.2023.111155. URL: https://www.sciencedirect.com/science/article/pii/S0010938X2300197X.

Department of Chemistry and Chemical Engineering
CHALMERS UNIVERSITY OF TECHNOLOGY
Gothenburg, Sweden
www.chalmers.se

CHALMERS
UNIVERSITY OF TECHNOLOGY